



**HAL**  
open science

## Thermomagnetically Responsive $\gamma$ -Fe<sub>2</sub>O<sub>3</sub>@Wax@SiO<sub>2</sub> Sub-Micrometer Capsules

Marion Baillot, Gauvin Hemery, Olivier Sandre, Véronique Schmitt, Rénal  
Backov

► **To cite this version:**

Marion Baillot, Gauvin Hemery, Olivier Sandre, Véronique Schmitt, Rénal Backov. Thermomagnetically Responsive  $\gamma$ -Fe<sub>2</sub>O<sub>3</sub>@Wax@SiO<sub>2</sub> Sub-Micrometer Capsules. *Particle & Particle Systems Characterization*, 2017, 34 (10), pp.1700063. 10.1002/ppsc.201700063 . hal-01610909

**HAL Id: hal-01610909**

**<https://hal.science/hal-01610909>**

Submitted on 5 Nov 2018

**HAL** is a multi-disciplinary open access archive for the deposit and dissemination of scientific research documents, whether they are published or not. The documents may come from teaching and research institutions in France or abroad, or from public or private research centers.

L'archive ouverte pluridisciplinaire **HAL**, est destinée au dépôt et à la diffusion de documents scientifiques de niveau recherche, publiés ou non, émanant des établissements d'enseignement et de recherche français ou étrangers, des laboratoires publics ou privés.

**Article type: Full Paper**

## **Thermo-Magnetically Responsive $\gamma$ -Fe<sub>2</sub>O<sub>3</sub>@Wax@SiO<sub>2</sub> Submicron Capsules**

*M. Baillot,<sup>[1]</sup> G. Hemery,<sup>[2]</sup> O. Sandre,<sup>[2]</sup> V. Schmitt<sup>[1,\*]</sup> and R. Backov<sup>[1,\*]</sup>*

[1] Centre de Recherche Paul Pascal, Univ. Bordeaux, CRPP-UPR CNRS 8641, 115 Avenue Albert Schweitzer, 33600 Pessac, France. Schmitt@crpp-bordeaux.cnrs.fr, backov@crpp-bordeaux.cnrs.fr  
schmitt@crpp-bordeaux.cnrs.fr, backov@crpp-bordeaux.cnrs.fr

[2] Laboratoire de Chimie des Polymères Organiques, Univ. Bordeaux, LCPO-UMR CNRS 5629, ENSCBP 16 avenue Pey Berland, F-33607 Pessac, France.

### **Abstract**

A three steps synthesis route is proposed to generate the first thermo-sensitive and magnetically responsive  $\gamma$ -Fe<sub>2</sub>O<sub>3</sub>@Wax@SiO<sub>2</sub> submicron capsules with a paraffinic core and a solid and brittle shell. The process integrates Pickering-based emulsions, inorganic and sol-gel chemistries to promote monodisperse in size wax droplets,  $\gamma$ -Fe<sub>2</sub>O<sub>3</sub> nanoparticles and mineralization of the wax/water interfaces. Final hybrid capsules are obtained with an average size around 800 nm, representing thereby the first example of sub-micrometer capsules generated employing Pickering emulsions as templates. Cetyltrimethylammonium bromide (CTAB) cationic surfactant added during mineralization at concentrations between 0.17 wt.% and 1.0 wt.% impact the shell density. The shell density seems to improve its mechanical strength while affording a low wax expansion volume without breaking for CTAB concentrations above 1.0 wt.%. On the contrary, for the lower CTAB concentration (0.17 wt.%), the silica shell becomes less bulky and cannot resist the wax dilatation induced by the solid-to-liquid phase transition imposed by hyperthermia. The magnetically-induced heating provided by the internal magnetic moments is sufficient to melt the wax core, expanding its volume, inducing thereby the surrounding silica shell rupture. Such  $\gamma$ -Fe<sub>2</sub>O<sub>3</sub>@Stearic Acid@Wax@SiO<sub>2</sub> submicron capsules allow a sustained wax release with time, whereby 20% of the wax is being released after 50 minutes of alternating magnetic field (AMF) treatment.

## 1. Introduction

Capsules-based technologies offering both confinement of the inner functional compounds and their stimuli-responsive release are the subject of highly competitive researches when considering their applications in the fields of medicine,<sup>[1,2]</sup> cosmetics<sup>[3,4]</sup> and agriculture.<sup>[5-7]</sup> Due to the wide scope of potential applications, tremendous varieties of capsules have been generated within the last decade. Not only capsules of different sizes were developed,<sup>[8]</sup> but also chemical nature and shapes were tried out, as for instance protein based vehicles,<sup>[9]</sup> cyclodextrins,<sup>[10]</sup> thermally gated liposomes,<sup>[11]</sup> colloidosomes,<sup>[12,13]</sup> silica shell microcapsules,<sup>[14-16]</sup> thermo-sensitive PNIPAM-silica nanocapsules,<sup>[17]</sup> thermo-sensitive hydrogel microspheres,<sup>[18]</sup> PNIPAM-poly(lactide) microsphere,<sup>[19]</sup> and so forth. Moreover the release dynamics can be adjusted to address various timescales, ranging from a continuous slow leakage over several hours driven by the Fick's diffusion<sup>[20]</sup> to instantaneous delivery.<sup>[21]</sup> To target an on-demand delivery, we have proposed the synthesis of crystallized wax cores surrounded by a silica shell, labelled Wax@SiO<sub>2</sub> capsules, able to open and release their content upon application of a soft thermal treatment.<sup>[22]</sup> In this system, the wax core volume expansion, during melting, promotes the breaking of the surrounding silica shell. The whole synthetic path combined advantageously Pickering emulsions<sup>[23,24]</sup> and sol-gel chemistry.<sup>[25]</sup> Later on, we extended the process to water-in-wax-in-water or wax-in-water-in-oil double emulsions to elaborate respectively Water@Wax@SiO<sub>2</sub><sup>[26]</sup> and Wax@Water@SiO<sub>2</sub><sup>[27]</sup> multi-cargo types of hybrid capsules. These last strategies offer higher potential for multi-tasks delivery, segregating the hydrophobic and hydrophilic moieties when trapped within the capsules, preventing thus their interaction prior to their delivery. While these synthetic routes offered advantages leading to final materials with interesting properties, two main issues were still to be treated. The first issue concerns the particle sizes, as up to now such capsules bearing diameters below the micrometer were never synthesized. The second issue to address

is of utmost importance, as the heat applied to induce the melted wax core release was macroscopic, meaning that we have had to heat the full capsules dispersion batch to induce the release. The challenge was then to conceive smaller capsules offering furthermore the capability of inducing a localized heat rather than using an external macroscopic one. As before, we used a Pickering-based wax-in-water emulsion. We prepared the emulsions using a microfluidizer to address the size issue, while making use of  $\gamma$ -Fe<sub>2</sub>O<sub>3</sub> superparamagnetic nanoparticles to promote an internal and local magnetically induced heating, known as the magnetic hyperthermia phenomenon under a radiofrequency magnetic field,<sup>[28,29]</sup> employed in diverse configurations in the literature either for tumor ablation or for magnetically induced drug delivery.<sup>[30,31]</sup> Considering organic-inorganic hybrid capsules reported in the recent literature, one can mention magnetic iron oxide nanoparticles present at the external corona of particles, as for instance with mesoporous silica bearing a hairy polymeric thermo-responsive shell,<sup>[32]</sup> or another type of microcapsules showing magnetically induced bursting,<sup>[33]</sup> or with a Pickering-based Water@ $\gamma$ -Fe<sub>2</sub>O<sub>3</sub>@SiO<sub>2</sub> nano-emulsion,<sup>[34]</sup> where magnetic hyperthermia was employed to catalyze the hydrolysis and release of a model pro-drug initially forming the oily core. In that case superparamagnetic nanoparticles (NPs) were localised precisely at the oil surface, below the mesoporous silica shell that is permeable to water.

In the present study, we used maghemite ( $\gamma$ -Fe<sub>2</sub>O<sub>3</sub>) superparamagnetic NPs coated with fatty acids (stearic acid SA or oleic acid OA) and dispersed in wax, this core being surrounded by a silica shell, resulting into thermo-magnetically responsive submicron capsules labelled hereafter  $\gamma$ -Fe<sub>2</sub>O<sub>3</sub>@Wax@SiO<sub>2</sub>.

## 2. Results and Discussion Section

The whole synthetic route of synthesizing  $\gamma$ -Fe<sub>2</sub>O<sub>3</sub>@Wax@SiO<sub>2</sub> capsules is depicted on **Figure 1**.

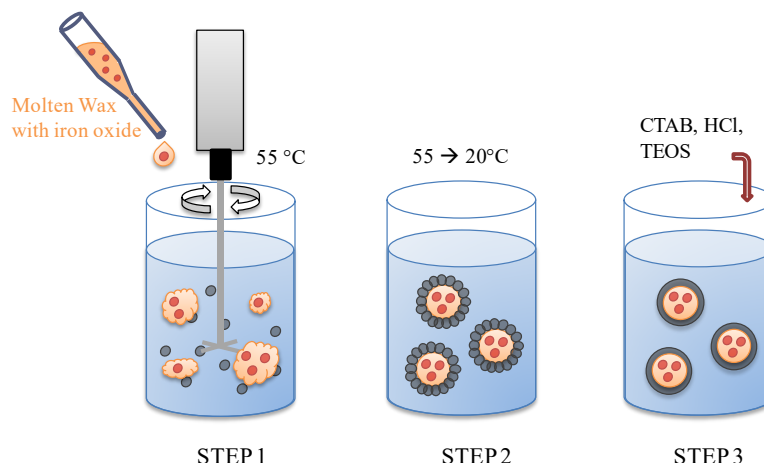


**Figure 1.** Scheme of the whole process used to obtain magnetically-responsive capsules. Step 1: Thanks to their fatty acid coating, a waxy paste of superparamagnetic iron oxide NPs dispersed in molten wax is emulsified at 55°C in presence of silica Aerosil™ A380 nanoparticles functionalized by electrostatic adsorption of a very low amount of cationic surfactant (CTAB below the CMC). Step 2: Once the limited coalescence phenomenon occurred and a monodisperse Pickering emulsion is obtained, temperature is decreased. Step 3: Sol-gel synthesis of a rigid and breakable silica shells around the wax crystallized droplets stabilized by silica nanoparticles.

The first step corresponds to the hybrid organic-inorganic paraffin phase formulation, containing molten wax and iron oxide NPs dispersed at optimized concentration, i.e. sufficient to induce the solid-liquid wax phase transition in the final particle suspension by magnetic hyperthermia while keeping colloidal stability. These  $C_1C_2S_3@OA$  NPs (see experimental section and **Figure 9** for the detailed explanation of the adopted notation) diluted in eicosane at 45°C, which correspond to the maximum reachable temperature for a measurement, exhibit an intensity-averaged hydrodynamic diameter of 20 nm with a polydispersity index (PDI) of 0.36 (as deduced from the 2<sup>nd</sup> order cumulant fit). Such low hydrodynamic diameter indicates that iron oxide NPs are most likely individually dispersed (rather than forming clusters), and covered by a self-assembled monolayer (SAM) of fatty acid molecules. The following step corresponds to the formulation of the magnetically doped eicosane-in-water direct emulsion with a narrow drop size distribution. Eicosane, containing the  $C_1C_2S_3$  fraction of iron oxide NPs coated by a SAM (of either OA or SA) is progressively dispersed into an aqueous dispersion of silica NPs previously rendered partially hydrophobic (**Figure 1.** step 1) and heated at 55 °C to avoid wax crystallization. The choice of using

Pickering emulsions is explained by two important reasons. At first, it is an easy way of generating wax droplets with good size monodispersity despite a turbulent flow processing at very high shear rates, taking advantage of the so-called "limited coalescence" process<sup>[35,36]</sup> Limited coalescence consists in producing a large excess of oil-water interface compared with the interfacial area that can be covered by the solid particles. As silica nanoparticles are irreversibly anchored at the wax-water interface, when stirring is stopped, the ongoing coalescence process stops as soon as all interfaces are sufficiently covered. Thus, Pickering emulsions are characterized both by narrow droplet size distribution and high kinetic stability. The second important feature is that the silica NPs adsorbed at the wax-water interface will serve as preferential nucleation sites when the sol-gel process occurs in the hydrophilic continuous phase (Figure 1. step 3).<sup>[14,22,26,27]</sup> As seen on **Figure S1 (Supporting Information)**, the droplet size distribution is very narrow and centred around 900 nm with PDI=0.05. We use a previously optimized protocol established for dodecane emulsification with a silica/oil weight ratio equal to  $35 \times 10^{-3}$ , where we obtained droplets with an average size of 7  $\mu\text{m}$ .<sup>[14]</sup> Assuming that all NPs were adsorbed, we defined the surface coverage  $C$  by a geometrical relation linking the amount of particles and droplets size:

$$C = \frac{m_{particles} \cdot D[3,2]}{4 \cdot d_p \cdot \rho_p \cdot V_d} \quad (1)$$

Where  $m_{particles}$  is the mass of particles,  $d_p$  their diameter,  $\rho_p$  their density,  $D[3, 2]$  the surface-averaged diameter of droplets, and  $V_d$  the total dispersed-phase volume. More precisely,  $C$  correspond to the ratio between the interfacial area that the particles may cover and the total interfacial area originating from the emulsion,  $S_{inter}$ , which is defined as  $S_{inter} = 6V_d/D[3, 2]$  with  $D[3, 2] = \sum_i D_i^3 / \sum_i D_i^2$ .<sup>[37]</sup> Then we can estimate the average amount of particle layers  $n$  by  $n = C/0.9$ , where 0.9 correspond to the coverage for a dense monolayer.<sup>[36]</sup> In our previous study, there were four layers of silica NPs covering the oil droplets. Using the same Aerosil™ A380/eicosane ratio with an organic phase at 18 wt.%, we obtained a dispersion with droplets

size equals to 900 nm and a surface coverage  $C= 0.6$ . Even if  $C$  is inferior to the 0.9 required for an optimal coverage, the obtained dispersion is stable over at least one week (**Supporting Information, Figure S1.**) when stored at room temperature ( $\approx 20\text{ }^{\circ}\text{C}$ ).

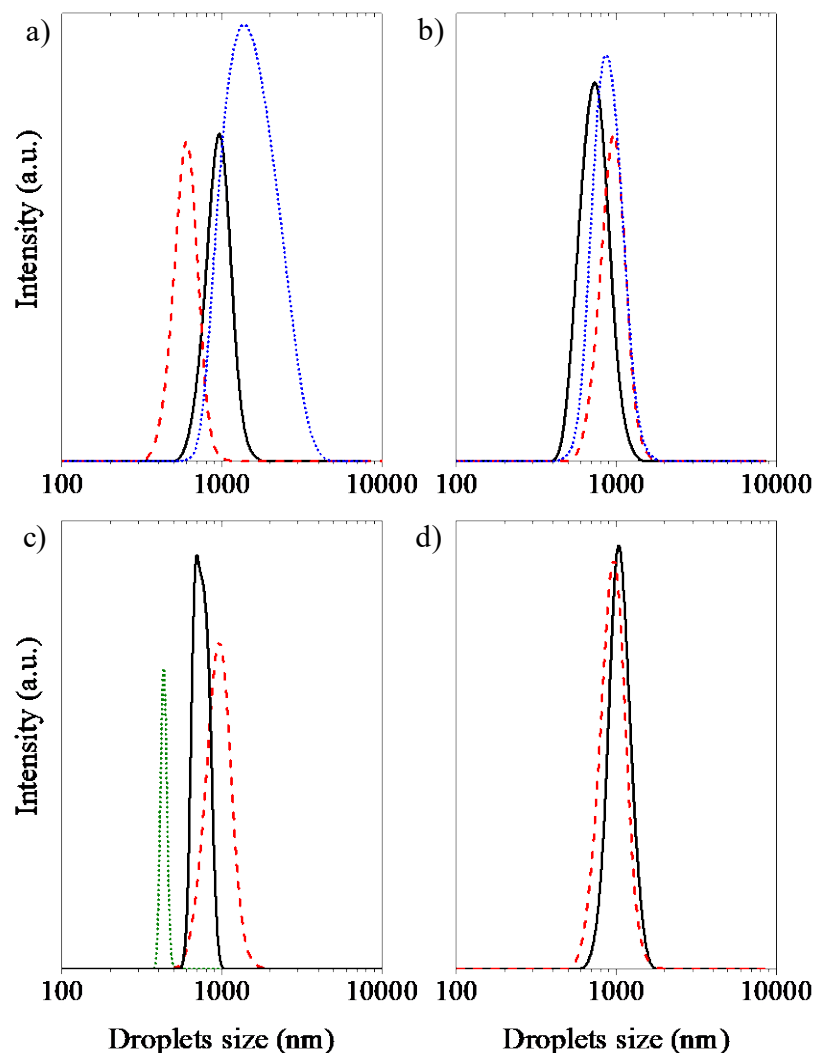


**Figure 2.** Drop size distributions measured by DLS of the wax-in-water emulsion stabilized with functionalized silica nanoparticles. a-b) Heating-cooling run was made to test the resistance of emulsion with surface coverage of a)  $C=0.6$  and b)  $C=1.02$ . The black line corresponds to the initial eicosane dispersion at  $20\text{ }^{\circ}\text{C}$ , the red dashed line corresponds to the eicosane dispersion heated at  $45\text{ }^{\circ}\text{C}$  and the blue dotted line corresponds to the eicosane dispersion cooled at  $20\text{ }^{\circ}\text{C}$ . c) Drop size distribution of the Pickering wax-in-water emulsion containing  $\text{C}_1\text{C}_2\text{S}_3@\text{OA}$  particles. The black thin line corresponds to the emulsion with  $\text{C}_1\text{C}_2\text{S}_3@\text{OA}$  and the green dotted line corresponds to the emulsion with  $\text{C}_1\text{C}_2\text{S}_3@\text{OA}$  where functionalized silica nanoparticles were added at the end of the emulsification process. Red dashed line corresponds to the reference emulsion. d) Drop size distribution of the Pickering wax-in-water emulsion containing  $\text{C}_1\text{C}_2\text{S}_3@\text{SA}$  particles (black line), without adding CTAB-coated  $\text{SiO}_2$  NPs in excess. The red dashed line corresponds to the reference emulsion.

Silica NPs used as wax-in-water emulsion stabilizers have been shown to withstand the volume expansion induced by melting during several freeze-thaw cycles.<sup>[38-40]</sup> So should the NPs used in the present paper do with the eicosane dispersion when heated above the eicosane melting temperature ( $T_m^{eicosane} \approx 35.9^\circ\text{C}$ ). However, a surface coverage of 0.7 is not sufficient to resist when the emulsion is heated from 20 to 45°C. This can be seen by the evolution of the drop size distribution after one heating (to 45°C)-cooling (back to 20°C) cycle. Indeed, the mean drop size has increased and a loss of monodispersity can be observed (**Figure 2.a**). Using a silica/eicosane weight ratio equal to  $59 \times 10^{-3}$ , we obtained an eicosane dispersion with the droplet mean size of 800 nm, with a PDI=0.015, but they much better resisted to the increase of temperature. In fact, droplet size had barely changed during the heating-cooling cycle (**Figure 2.b**). Assuming again that all the CTAB-coated SiO<sub>2</sub> NPs are adsorbed at the drop surface, as the drops size is unchanged, it can be deduced that the drops are better covered (C=0.9), which could explain the better resistance to freezing-thaw cycles. We also addressed the iron oxide NP coating effect over the emulsion stabilization. Oleic acid grafted iron oxide NPs (C<sub>1</sub>C<sub>2</sub>S<sub>3</sub>@OA) were dispersed into the organic phase above melting temperature at a concentration of 12 g·L<sup>-1</sup> of iron oxide. Right after emulsification, the droplet intensity-averaged hydrodynamic size obtained was 740 nm with a PDI = 0.019. However this emulsion was aggregated the next day. Two hypotheses may explain this phenomenon. The first assumption is that the droplets were subject to partial coalescence. Indeed, it is a common destruction mechanism for emulsions composed of a crystallisable phase.<sup>[41-43]</sup> Since the dispersed phase contained paraffin crystals, the droplet surfaces could have irregularities such as facets or spikes as recently reported by Denkov et al.<sup>[44]</sup> During crystal growth, and even above the main melting temperature in the domain of rotator phase pre-transition, the energy of crystal lattice can exceed the interfacial tension and lead to the formation of still fluid but non-spherical drops.<sup>[44]</sup> Then a microcrystal, protruding from a crystalline drop can

apply sufficient pressure at the interface of another drop and trigger their sticking together. The oil then comes in contact, wetting the crystals, which will reinforce the connection through capillary bridges and thus create a sufficiently connected network, preventing the restoration of the initial emulsions. In order to avoid this phenomenon, a small amount of functionalized silica NPs was added, in excess, at step 2 to increase the surface coverage fraction  $C$  and the resistance of the droplets previously formulated by the emulsification process (**Figure 2.c**). The resulting dispersion was stored in a controlled temperature chamber at 20 °C. The droplet intensity-averaged size was decreased to 450 nm with a PDI = 0.0013 and  $C=0.36$ . The second assumption is that the aggregation is the result of the destabilization of oleic acid-coated iron oxide NPs. In fact, over time it has been more and more difficult to disperse the dry  $C_1C_2S_3@OA$  magnetic paste in wax, presumably as a result of ageing. Initially highly volatile brown  $C_1C_2S_3@OA$  particles turned with time into irreversibly black powdery blocks. For a better stability, we changed the coating from oleic acid to stearic acid (**Figure 2.d**) and we characterized the  $\gamma\text{-Fe}_2\text{O}_3@SA@Wax$  emulsion in water without addition of silica NPs in excess at step 2 of the formulation. We determined by TGA that the organic part in the magnetic paste was 22 wt.% (**Supporting Information, Figure S2**). As ascribed from its high melting point (69.3°C while the melting point of oleic acid is 13°C), this new coating does not allow rotational movement of the carbon-carbon bonds in its alkane chain. Thus, it reduces the interactions between iron oxide NPs during storage. In addition, the saturated aliphatic chains are insensitive to oxidation, which extends also their shelf life; unlike the ones coated with oleic acid, several months later the  $C_1C_2S_3@SA$  NPs were still readily dispersible in molten wax. The resulting dispersion did not require additional CTAB-coated silica NPs after its formulation (besides the initial quantity introduced at the beginning of step 1). In order to induce the release at the desired time, it was mandatory to form a shell at the water-wax interface. Indeed the better particle-covered drops withstand heating-cooling

cycles and a fragile shell that does not support the mechanical stress arising from the wax volume expansion under heating is necessary. Under optimized conditions, this brittle and solid shell would bring greater stability to the emulsions and better storage stability, while still allowing the wax release when heated above to the melting point of the wax, as ascribed to its volume thermal expansion.

## 2.1. Influence of the CTAB concentration on the Pickering emulsion-based capsules

During the sol-gel process (step 3), CTAB is used to favor the  $\text{Si(OH)}_4$  condensation kinetics. This cationic surfactant is known for its influence over the formation of MCM-41 meso-structured matrix where meso-structured  $\text{SiO}_2$  grains heterogeneously nucleated at the external surface of microscopic dodecane droplets.<sup>[14,45]</sup> In order to determine the effect of the CTAB in the present case, two different concentrations of CTAB (0.17 and 1.0 wt.%) were added during the sol-gel process (**Figure 3**), performed in acidic catalytic conditions.

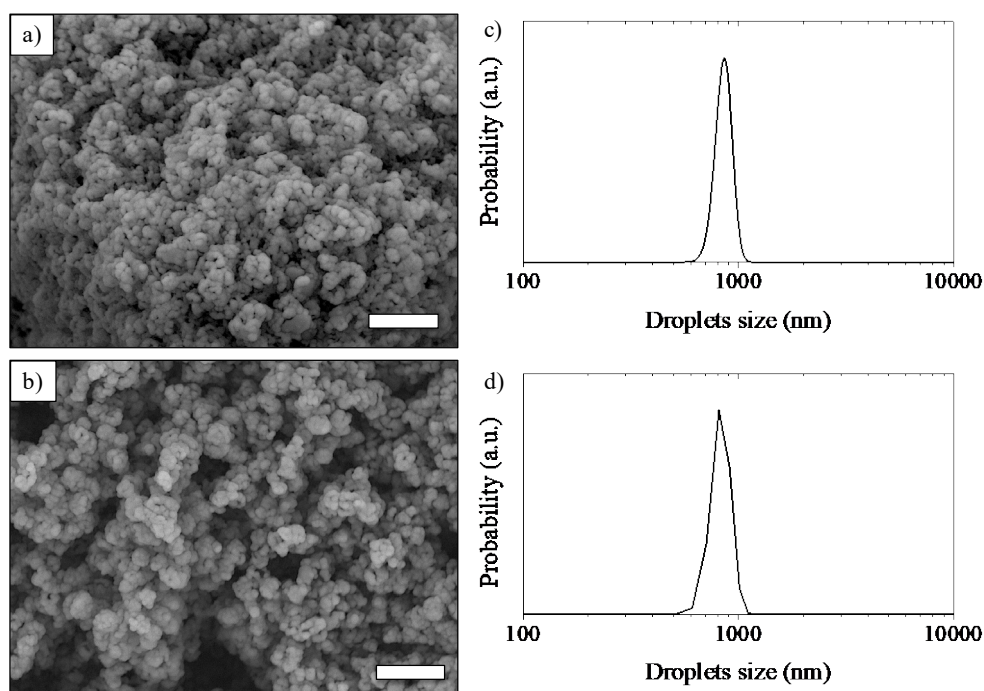


**Figure 3.** SEM pictures of dried capsules obtained from Eicosane-in-Water emulsion containing  $\text{C}_1\text{C}_2\text{S}_3@SA$  magnetic NPs with various concentration of CTAB during the mineralization step 3: a) 0.17 wt.% CTAB and b) 1.0 wt.% CTAB. Scale bar = 10  $\mu\text{m}$ . c-d) Corresponding size distributions of the two dried capsules as measured by image analysis and particle counting. The mean surface diameter is 825 nm for both samples with a standard deviation of 0.06 %.

When considering the **Figure 3** we can notice that the “native”  $\gamma\text{-Fe}_2\text{O}_3@\text{Wax}@SiO_2$  hybrid capsules are quite monodisperse in size with a diameter centred around 825 nm and a standard deviation of 0.06 % whatever the amount of CTAB employed during the synthetic path. The size distribution was determined by statistical analysis using the ImageJ free software over 200 capsules after stirring and washing steps. Using TEM image analysis, we determined (after washing capsules with THF) that the shell thickness with both concentrations was equal to  $41 \pm 5$  nm (**Figure 4.a**). On the first hand, we observed that the CTAB concentration has no influence over the shell thickness. However, with 0.17 wt.% of CTAB the obtained capsules tend to cream whereas with 1.0 wt.% CTAB, they tend to sediment. On the other hand, we found by using helium pycnometry, values of capsule shell density equal to 1.3 and 2.3  $\text{g}\cdot\text{cm}^{-3}$  when employing respectively 0.17 and 1.0 wt.% CTAB. Those results are in adequacy with the sedimentation/creaming speed of drops (**Figure 4.b**)  $V$ , which can be estimated through:

$$V = \frac{2g}{9\eta} \frac{R^2}{\left(1 + \frac{e}{R}\right)} \left[ (\rho_{\text{wax}} - \rho_{\text{silica}}) + \left(1 + \frac{e}{R}\right)^3 (\rho_{\text{silica}} - \rho_{\text{water}}) \right] \quad (2)$$

This expression simply derives from the fundamental dynamic equation in the stationary state considering weight, buoyancy and friction. Here,  $g$  is the gravity acceleration ( $\approx 9.81 \text{ m}\cdot\text{s}^{-2}$ ),  $\eta$  the fluid dynamic viscosity of the dispersed phase,  $R$  the droplet radius,  $e$  the shell thickness,  $\rho$  the volumetric mass density of wax/silica/water phase respectively indicated as index. We choose the following convention: if the speed is negative, capsules move up and the suspension exhibits creaming. On the contrary, if the speed is positive, capsules move down and settle. Creaming and sedimentation compensate when  $V = 0$ , *i.e.* when following condition is fulfilled:

$$\frac{e}{R} = \sqrt[3]{\frac{\rho_{\text{silica}}^* - \rho_{\text{wax}}}{\rho_{\text{silica}}^* - \rho_{\text{water}}}} - 1 \quad (3)$$

If we observed the **Figure 4.a** for a density of  $1.3 \text{ g}\cdot\text{cm}^{-3}$ , the speed is positive and for a density of  $2.3 \text{ g}\cdot\text{cm}^{-3}$  it becomes negative in agreement with the experimental results. An intermediate concentration of CTAB (0.5 wt.%) was also used, but the obtained  $\gamma\text{-Fe}_2\text{O}_3@\text{Wax}@\text{SiO}_2$  capsules were at the perfect balance with the medium, rendering the washing step by centrifugation-redispersion difficult. For a CTAB concentration of 0.5 wt.% since no creaming or sedimentation has been observed, we can consider that  $V = 0$  which corresponds to a density of around the perfect balance value  $\rho_{\text{silica}}^* = 1.8 \text{ g}\cdot\text{cm}^{-3}$  where we have assumed that the capsule size and thickness is the same as those measured for the two other CTAB concentrations. Those results are in adequacy with a previous study,<sup>[14]</sup> when the CTAB concentration is higher, the formed silica shell density formed by the mineralization process increases while consuming a higher amount of TEOS precursor.

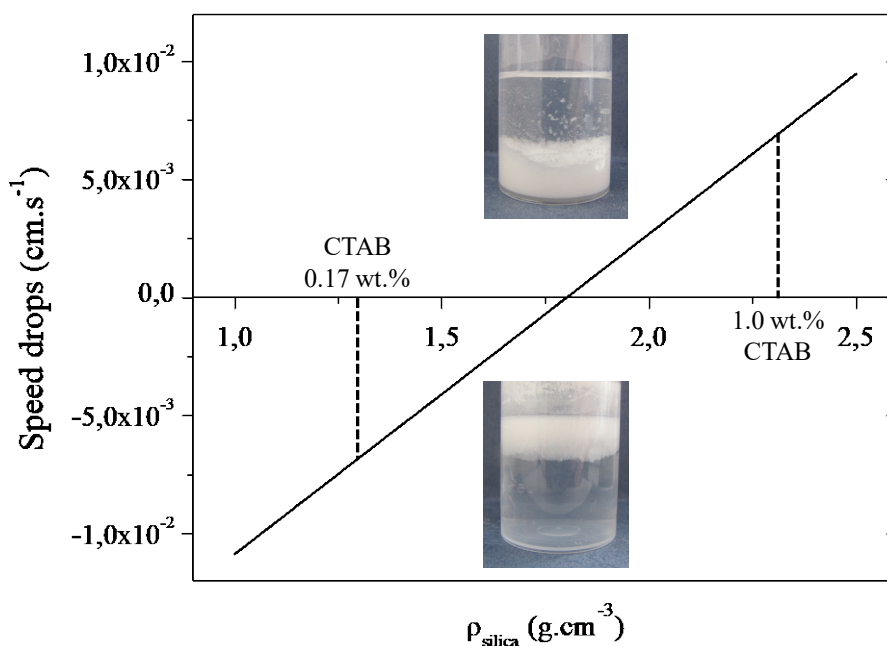


**Figure 4.** Calculated drop speed using Eq. 2 *versus* the silica shell density, measured by helium pycnometry, for capsules synthesized using 0.17 and 1 wt.% CTAB concentrations with respectively measured silica shell densities of  $1.3$  and  $2.3 \text{ g}\cdot\text{cm}^{-3}$ . The sediment part is indicated in the grey area. The creaming part is indicated in the orange area. The capsules size and thickness are considered unchanged and equal to  $825 \text{ nm}$  and  $41 \text{ nm}$  respectively

## 2.2. Influence of the superparamagnetic nanoparticles concentration over the wax melting process

To achieve the goal of a magnetically induced release of the wax or of another lipophilic cargo encapsulated inside the silica submicron shells by microscopically localized heat, the priority synthesis of well-defined magnetic nanoparticles was mandatory. Using an alkaline co-precipitation procedure in water followed by an electrolyte-mediated magnetic size sorting procedure described in the materials and methods section, superparamagnetic iron oxide NPs were obtained. To trigger the release of the encapsulated wax, magnetic NPs with high heating efficiency are needed; therefore large sizes ranging from 12 to 15 nm were selected after the size-sorting process. The specific area ( $S_{\text{spe}}$ ) for those NPs was in the 80 – 100  $\text{m}^2\cdot\text{g}^{-1}$  range as calculated from the approximate diameter observed on TEM images. Experimental determination of the specific area of C<sub>1</sub>C<sub>2</sub>S<sub>3</sub>@SA NPs by Porod's formula applied on their small angle neutron scattering (SANS) curve (**Supporting Information, Figure S8**) yielded  $S_{\text{spe}}=110 \text{ m}^2\cdot\text{g}^{-1}$ , corresponding to an average SANS diameter of ~11 nm. Nanoparticles size has an important effect because the larger the size, the greater the heating power under an alternating magnetic field (AMF), as estimated from the specific absorption rate (SAR).<sup>[29]</sup> However, the disadvantage of large NPs is the higher difficulty to disperse individually in the wax (i.e. not as clusters). This was overcome by the SA coating. In addition, the physically blocking of the nanocrystals when confined in the wax lead to the loss of the so-called “Brown relaxation” contribution of magnetically induced thermal losses under an applied AMF. Moreover, the largest diameters in the distribution (~15 nm) also approach the superparamagnetic-ferromagnetic size threshold, meaning that some of these magnetic NPs can exhibit coercivity. Thereby it is necessary to use an AMF intensity above the anisotropy field to induce heating.<sup>[29]</sup> In order to determine the most compatible systems, and given the constraints, the SAR of the uncoated C<sub>1</sub>C<sub>2</sub>S<sub>3</sub> cores was determined by preliminary tests in water (at acidic pH) and then again after their dispersion in the eicosane wax; these results are summarized in **Table 1**.

**Table 1.** Summary of specific absorption rate (SAR) values under an AMF at 755 kHz of 10.2 kA·m<sup>-1</sup> intensity for the C<sub>1</sub>C<sub>2</sub>S<sub>3</sub> fraction of iron oxide NPs, dispersed in water, and dispersed in eicosane wax after coating with either oleic acid (OA) or stearic acid (SA). SAR values were calculated using the tabulated values of the corresponding dispersing medium for the sample heat capacity, respectively  $C_p^{\text{Water}} = 4.18 \text{ J}\cdot\text{g}^{-1}$ ,  $C_p^{\text{Eicosane}} = 1.88 \text{ J}\cdot\text{g}^{-1}$  in solid state (25°C), and  $C_p^{\text{Eicosane}} = 2.27 \text{ J}\cdot\text{g}^{-1}$  in the liquid state (40°C).<sup>[42]</sup>

Sample name	Concentration (g·L <sup>-1</sup> iron oxide)	Solvent	SAR (W·g <sup>-1</sup> iron oxide)
C <sub>1</sub> C <sub>2</sub> S <sub>3</sub>	4	Water (HNO <sub>3</sub> pH~2)	280
C <sub>1</sub> C <sub>2</sub> S <sub>3</sub> @OA	2	Eicosane (Solid)	8
C <sub>1</sub> C <sub>2</sub> S <sub>3</sub> @OA	4	Eicosane (Solid)	13
C <sub>1</sub> C <sub>2</sub> S <sub>3</sub> @OA	6	Eicosane (Solid)	7
C <sub>1</sub> C <sub>2</sub> S <sub>3</sub> @OA	12	Eicosane (Solid/Liquid)	4-2
C <sub>1</sub> C <sub>2</sub> S <sub>3</sub> @SA	12	Eicosane (Solid/Liquid)	6-4

To disperse these C<sub>1</sub>C<sub>2</sub>S<sub>3</sub> NPs in wax, they were firstly conferred a hydrophobic surface thanks to fatty acid coating. The nanoparticles grafted either with oleic or stearic acid were dispersible in molten wax, with low values of the hydrodynamic diameter indicating the absence of aggregates. The organic content in the dried magnetic paste was assessed by TGA (**Supporting Information, Figure S2.**). Oleic acid is a commonly used ligand employed in the synthesis of magnetic iron oxide nanoparticles by thermal decomposition.<sup>[29]</sup> It is also used as a surfactant to transfer iron oxide NPs synthesized by the aqueous route into organic solvents, thanks to the strong chemisorption of the carboxylic acid moiety onto the nanocrystalline iron oxide surface. We determined that the organic content in the dry C<sub>1</sub>C<sub>2</sub>S<sub>3</sub>@OA paste is 13 wt.% (**Supporting Information, Figure S2.a**). In this way, we can evaluate the specific heating power under radiofrequency magnetic field of the C<sub>1</sub>C<sub>2</sub>S<sub>3</sub>@OA NPs dispersed in eicosane at varying concentration (2, 4, 6 and 12 g·L<sup>-1</sup>), starting from a temperature below the melting point of eicosane, as seen in table 1. For concentrations lower than 12 g·L<sup>-1</sup>, a trend of SAR decrease with increasing concentration can be ascribed to partial

aggregation inducing dipolar magnetic interaction between the magnetic NPs responsible for SAR lowering. More importantly for the work, no macroscopic solid-to-liquid phase transition was observed. The temperature profile, as followed by a fiber optic sensor, was in agreement with visual observation and in situ DLS measurement (data not shown). Indeed, the melting temperature has never been exceeded or reached. We also determined by DSC that, whatever the applied heating rate, and despite the high concentration of fatty acid grafted iron oxide NPs, their presence had no influence on the melting temperature of the wax (35.9 °C) (Figure 5.a-b).

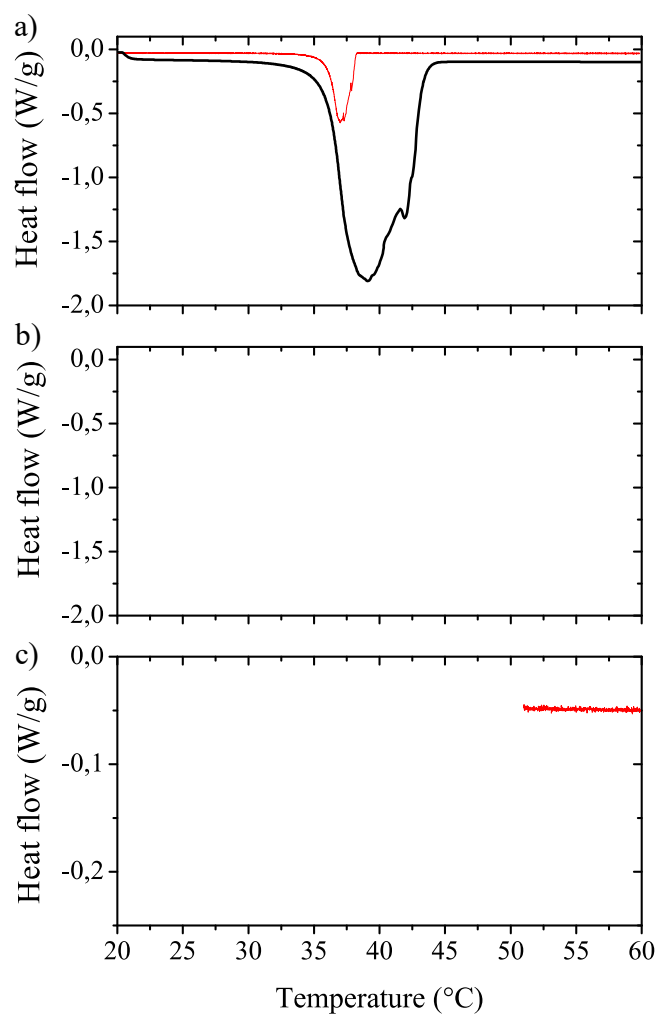


**Figure 5.** DSC thermograms of a) pure eicosane, b) eicosane doped with C1C2S3@SA NPs ( $12 \text{ g}\cdot\text{L}^{-1}$ ), and c)  $\gamma\text{-Fe}_2\text{O}_3(\text{SA})@\text{Wax}@\text{SiO}_2$  capsules in water. The black thick and red thin lines correspond respectively to  $2.0 \text{ }^\circ\text{C}/\text{min}$  and  $0.2^\circ\text{C}/\text{min}$  heating rates. For all samples, the transition occurs at  $T_m^{\text{onset}} = 35.9 \text{ }^\circ\text{C}$ .

Considering the  $\gamma\text{-Fe}_2\text{O}_3@\text{Wax}@\text{SiO}_2$  capsules dispersed in water, the melting onset temperature was still found at 35.9°C. The spread of the heat flux peak over a lower temperature range might be simply attributed to a lower quantity of materials having thermal transition (**Figure 5.c**). The thinner endothermic peak is certainly also related to the external amorphous silica shell with much higher intrinsic heat capacity  $C_p^{\text{silica}}=12.07 \text{ J}\cdot\text{g}^{-1}\cdot\text{K}^{-1}$  (at 295K)<sup>[46]</sup> than the wax core  $C_p^{\text{eicosane}}=1.88 \text{ J}\cdot\text{g}^{-1}\cdot\text{K}^{-1}$  for n-eicosane (at 298.4 K)<sup>[47]</sup>, which may contribute to squeezing of the wax melting temperature range. On the one hand, determining by DSC the wax melting temperature evolution when adding  $\gamma\text{-Fe}_2\text{O}_3$  NPs into the wax that is dispersed as submicron particles surrounded by a more or less dense silica shell is important information about the materials structural properties. In particular the absence of capillary induced melting point depression reported for n-eicosane confined in silica mesopores shows that eicosane molecules in this system are neither confined nor nano-structured (following Gibbs-Thomson equation).<sup>[48]</sup> On the other hand, we bear in mind that in the DSC experiments the heat flux is coming from the external environment of the capsules, while under magnetic hyperthermia it would come from their interior (i.e. by conversion of magnetic energy into thermal losses). Then, the macroscopic rising temperature determined in a bulk dispersion of  $\gamma\text{-Fe}_2\text{O}_3@\text{Wax}@\text{SiO}_2$  in water, through the magnetic hyperthermia process, might not correlate with the microscopic local heating temperature (and wax melting phase transition) reached within the capsules core, especially in the transient state (i.e. before reaching the temperature plateau). This is why temperature may not have reached the wax melting temperature macroscopically, while microscopically, within the capsules, it could be indeed the case. In this regard, we have to investigate the magnetic hyperthermia process step by step. The first step is the  $\gamma\text{-Fe}_2\text{O}_3\text{-Wax}$  composites bulk behaviour, i.e. not emulsified in water neither surrounded by a silica shell but just as a macroscopic (bulk) sample of 400  $\mu\text{L}$  volume (quartz cell). Considering **Figure S3 (Supporting Information)**, for a concentration

of  $12 \text{ g}\cdot\text{L}^{-1}$  of iron oxide NPs coated by OA and dispersed in eicosane in bulk wax, the magnetic field-induced hyperthermia allows exceeding the melting temperature. At first, the glass double-wall water-jacket set at  $37^\circ\text{C}$  was employed to stabilize the temperature of the sample at around  $33.5^\circ\text{C}$ . The fiber optic sensor detected two temperature stages. The first one was observed at  $36^\circ\text{C}$ , and reflects the wax solid-to-liquid phase transition with a smooth phenomenon of latent heat; the second was observed at  $38^\circ\text{C}$  suggesting an interaction between wax and iron oxide nanoparticles. In complement with measurement of temperature through time, the DLS signal was also used to observe these variations of physical states. The backscattered intensity of the laser beam varied depending whether the sample was solid or liquid. Indeed, wax crystals exhibit refractive index much different from the wax at liquid state and they scatter the laser beam, leading to an unstable signal as long as the system is biphasic (at the coexistence temperature between solid and liquid wax) or still solid. The complete transition to the liquid state, indicated by a recovered homogeneity of the system, resulted in a peak of the average beam intensity when obtaining a stable signal at the molten state. Moreover we noticed the presence of two peaks in the DLS signal (**Supporting Information, Figure S3.a**). The first one appeared when the sample temperature reached  $36^\circ\text{C}$  and was followed by an intermediary plateau. The second peak was present at  $38^\circ\text{C}$  which is in perfect correlation with results obtained with the temperature monitoring using the fiber optic sensor. This experiment was repeated three times consecutively (**Supporting Information, Figure S3.b-c**). The temperature evolution followed the same trend than during the first measurement with imposed radiofrequency magnetic field. However, the laser intensity fluctuated more at lower temperatures, presumably because the sample contained more heterogeneities in its frozen state. The wax structural rearrangement on heating and cooling depends on the heating and cooling rates and can be related to the wax and iron oxide heat capacities, the iron oxide heat capacity being about thrice lower at  $0.65 \text{ J g}^{-1}\cdot\text{K}^{-1}$  at  $298$

K.<sup>[49]</sup> In order to determine the role of the iron oxide NPs in these rearrangements, we heated macroscopically the Wax- $\gamma$ -Fe<sub>2</sub>O<sub>3</sub> composite, using the glass double-wall water-jacket as an external, non-magnetic, heating source. After stabilizing the sample temperature at an initial temperature near 31°C, we directly increased the temperature of the glass water-jacket from 37°C to 50°C for the first run (**Supporting Information, Figure S4.a**), then progressively for the second run (**Supporting Information, Figure S4.b**). In both cases, we still observed a temperature stage at 36°C and a change of slope around 38°C. Using DLS, we observed the same trend than when the AMF was applied, with a stabilization of the laser beam at 36°C and a peak at 38°C. That is the proof that the wax microscopic structure change is independent on the heat source, being either internally driven by the magnetic hyperthermia effect, or externally induced by the glass-jacket. The reverse experiments have been done by cooling the sample using the water-circulation from 50 to 35°C (**Supporting Information, Figure S4.c and d**). In that case, there was no peak for the DLS laser signal, and no slope change for the temperature curve at 38°C. In this configuration, the  $\gamma$ -Fe<sub>2</sub>O<sub>3</sub> nanoparticles trapped within the wax volume bearing a lower heat capacity than the surrounding matrix might act as hot spots that will lower the crystallization temperature of the wax in their vicinity, cancelling the DLS peak observed at 38°C. This effect has already been observed elsewhere with wax and asphaltens when dealing with bitumen-bees morphosyntheses.<sup>[50]</sup> Effectively at the intrinsic wax melting temperature (35.9°C), we observed the same effect by heating the wax either macroscopically or by magnetic field where  $\gamma$ -Fe<sub>2</sub>O<sub>3</sub> nanoparticles can behave as “hot spots” but have no interplay on the wax melting temperature. All observations made over the wax microstructure evolution with temperature by DSC experiments are not direct. The direct structural evidence comes actually from wide-angle X-ray scattering. All the WAXS experiments are presented and commented within the supplemental information (**Supporting Information, Figures S5 and S6**). In brief, we discuss a phenomenon of “pre-

transition” through the transient existence of a metastable “rotator” phase that has been described with eicosane.<sup>[51]</sup> The apparent heat capacities, due to a latent heat effect, increases and may play a role in the additional thermal phenomenon observed with an internal heating by magnetic hyperthermia, due to the incorporated magnetic “nano-heaters” as, compared to an external heating.<sup>[51]</sup>

### 2.3. Magnetic hyperthermia induced release of capsule core content

In order to achieve magnetically induced capsule-breaking, dual magneto- and thermo-sensitive capsules were exposed to an alternating magnetic field (AMF) of  $10.2 \text{ kA}\cdot\text{m}^{-1}$  intensity oscillating at 755 kHz, using the radiofrequency generator and application coil. Localized internal heating (as opposed to macroscopic external) and on-demand wax release were required, therefore a sufficiently concentrated suspensions of  $\gamma\text{-Fe}_2\text{O}_3@\text{Wax}@\text{SiO}_2$  capsules in water (prepared either with OA or SA coating of the magnetic NPs and at varying CTAB concentration) were placed in a 400  $\mu\text{L}$  quartz cuvette in the coil of the heating device. As for the previous experiments with bulk eicosane, the temperature of the samples was initially stabilized at  $32^\circ\text{C} \pm 2^\circ\text{C}$ , using the glass water-jacket (the circulating bath temperature being set at  $37^\circ\text{C}$ ). Then, the AMF was switched on and elevation of temperature was recorded employing the fiber optic sensor. As the capsules induce a strong scattering of the laser beam, they would necessitate long time channels and accumulation time of the autocorrelator to be measured by DLS (whereas temperature would vary too significantly during a sub-run). Therefore, intensity was not recorded versus time. With the capsule sample prepared using 0.17 wt.% CTAB ( $\rho_{\text{silica}}=1.3 \text{ g}\cdot\text{cm}^{-3}$ ), the temperature within the cuvette increased progressively (**Figure 6.a-b**), but not continuously. Before stopping the application of the magnetic field, we noted that the sample temperature containing the  $\text{C}_1\text{C}_2\text{S}_3@\text{SA}@\text{Wax}@\text{SiO}_2$  capsules started to decrease (**Figure 6.b**), while this phenomenon was less pronounced for the  $\text{C}_1\text{C}_2\text{S}_3@\text{OA}@\text{Wax}@\text{SiO}_2$  containing capsules, resulting in a

constant temperature at the end of the experiment (**Figure 6.a**). This observation is likely ascribed to a phenomenon of latent heat in the sample, certainly related with the endothermic wax melting process that consumes part of the magnetically-induced local heat. For capsules prepared using 1.0 wt.% CTAB ( $\rho_{\text{silica}}=2.3 \text{ g}\cdot\text{cm}^{-3}$ ), the temperature was stable during all the experiment (several tens of minutes). At first glance it means that there was no effect of the magnetic field (**Figure 6.c-d**) over the samples temperature, but this needs to be carefully interpreted. As we already discussed, this is not because the macroscopic temperature is apparently constant that locally (inside the capsules) the wax has not melted. Furthermore, with 1.0 wt% of CTAB, the surrounding silica shell is denser, a feature that may limit the heat transfer from inside the capsules toward the outside (silica being known as a good thermal insulator).

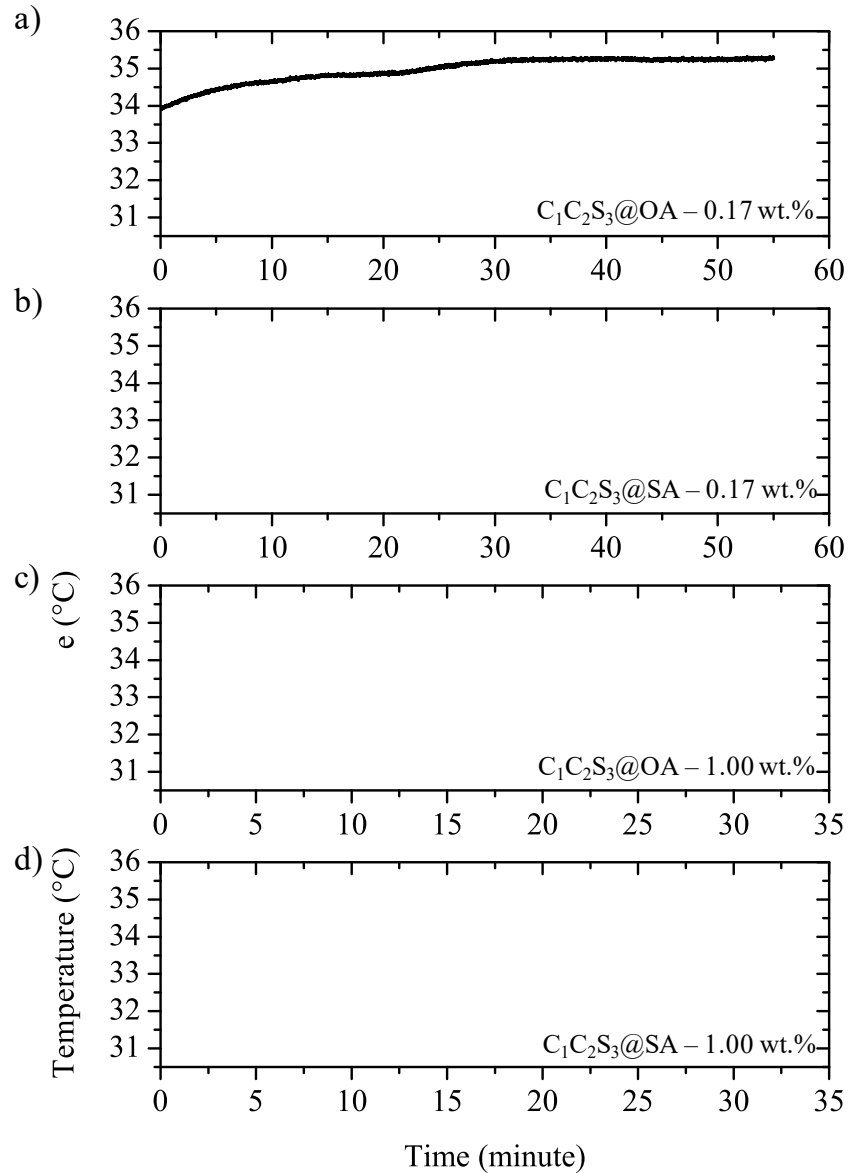


**Figure 6.** SAR determination of capsules dispersed in water under magnetic hyperthermia. a)  $C_1C_2S_3@OA@Wax@SiO_2$  particles in capsules with a shell synthesized at 0.17 wt.% of CTAB, b)  $C_1C_2S_3@SA@Wax@SiO_2$  particles in capsules with a shell synthesized at 0.17 wt.% of CTAB, c)  $C_1C_2S_3@OA@Wax@SiO_2$  particles in capsules with a shell synthesized at 1.0 wt.% of CTAB, d)  $C_1C_2S_3@SA@Wax@SiO_2$  particles in capsules with a shell synthesized with 1.0 wt.% of CTAB. The overall iron oxide concentration was kept constant for all experiments ( $12 \text{ g}\cdot\text{L}^{-1}$ ).

As we measured only the temperature in bulk with the fiber optic sensor, and not directly inside the capsules, the exact temperature of the sample core was unknown. We kept all the samples submitted to either alternating magnetic field or to macroscopic heating for SEM observations (**Figure 7**). For a better comparison, samples were observed before and after heating. At the lowest concentration of CTAB (0.17 wt.%), the magnetic field offered

the desired effect, meaning that it provoked the shell breaking and wax release of the synthesized capsules, for the SA-coated magnetic NPs. For the highest CTAB concentration (1.0 wt.%), the applied magnetic field had no apparent effect on the sample morphology. We then applied heat externally to reach a macroscopic temperature far above the wax melting point, but we still did not observe the wax release (**Figure 7.b**). This implies that a high-density shell ( $\rho_{\text{silica}}=2.3 \text{ g}\cdot\text{cm}^{-3}$ ) offers a mechanical strength high enough to withstand the volume expansion associated with the core melting.

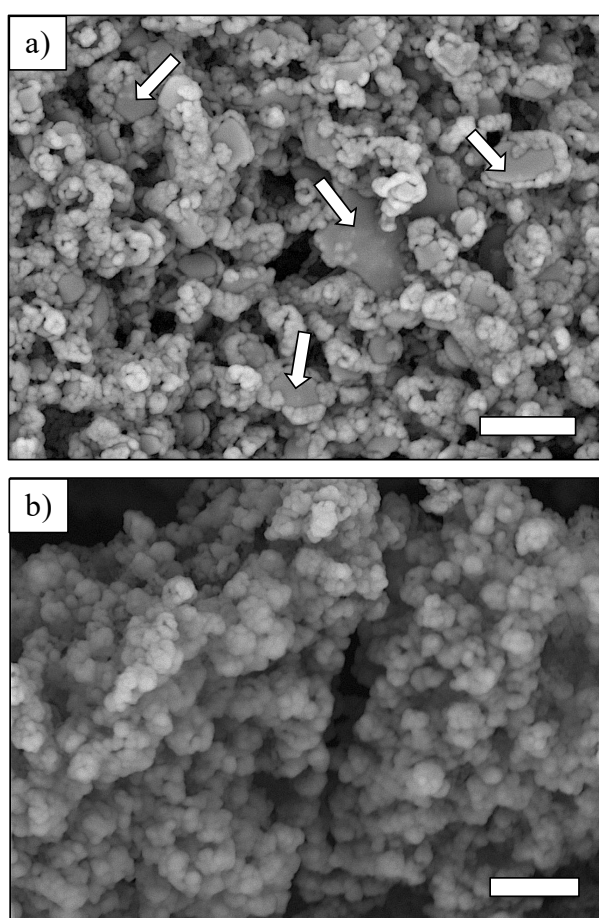


**Figure 7.** SEM pictures of  $\gamma\text{-Fe}_2\text{O}_3@SA@Wax@SiO_2$  capsules dried after magnetic hyperthermia that were obtained from Eicosane-in-Water emulsion at two concentrations of CTAB employed during the mineralization step 5: a) 0.17 wt.% ( $\rho_{\text{silica}}=1.3 \text{ g}\cdot\text{cm}^{-3}$ ) and b) 1.0 wt.% CTAB ( $\rho_{\text{silica}}=2.3 \text{ g}\cdot\text{cm}^{-3}$ ). Arrows indicate wax leakages from the broken shells. Scale bars = 10  $\mu\text{m}$

#### 2.4. Quantitative wax release assessment from the capsule cores induced by localized magnetic hyperthermia

Since it was possible to promote the release of the capsule core content by magnetic field hyperthermia, it sounded important to quantify the wax release profile *versus* time. In order to determine if this amount of wax depends on the exposure time under magnetic hyperthermia, the AMF application duration has been varied: 600, 1380, 2100, 3000 and 7200 s. The experiments were carried out twice for each time exposure on  $\gamma$ - $\text{Fe}_2\text{O}_3@SA@Wax@SiO_2$  capsules obtained at 0.17 wt.% CTAB concentration ( $\rho_{\text{silica}}=1.3 \text{ g}\cdot\text{cm}^{-3}$ ). As eicosane is soluble in chloroform while chloroform cannot diffuse through the silica shell, we used this solvent to extract the wax released by the capsules dispersed in water after a given AMF application time. This organic fraction was separate from the aqueous suspension. After dry extracts have been realized in an oven at  $75^\circ\text{C}$  during 6 h, we calculated the global amount of wax released, taking into account the amount of capsule for each samples. This experiment was made three times on several known concentrations of wax, being able to recover the exact expected concentration. As can be seen on **Figure 8**, the amount of wax released was around 20% after a time exposure of 50 minutes (3000 s), reaching 40% for longer times (2 hours).

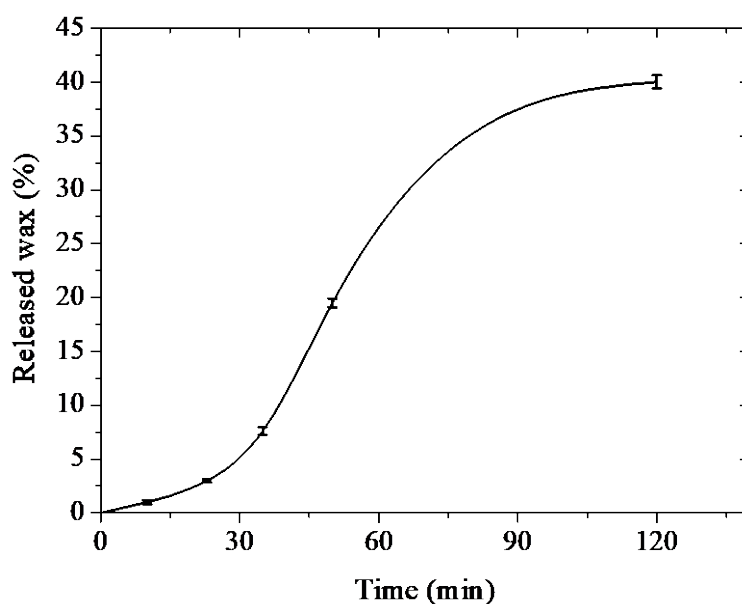


**Figure 8.** Evaluation of the amount of released wax *versus* magnetic field application time on  $\gamma$ - $\text{Fe}_2\text{O}_3@SA@Wax@SiO_2$  capsules. The plain line is used only as visual guide. The curve

can also be well fitted (with correlation coefficient  $R=0.992$ ) by the Weibull function of following parameters:  $42.35\% \cdot (1 - \exp(-0.00032 \cdot t^{1.876}))$ . Such phenomenological law has been reported in literature to describe the release kinetics of insoluble drugs.<sup>[52,53]</sup>

As can be seen from the release profile, it seems that there is an induction time. Indeed one expect the release not to be instantaneous as heating has to melt the inner wax, then the shell fracture has to occur and lastly the wax has to come out from the capsules. After this delay the release rate goes through a maximum and then is slowed down, reaching a plateau value of wax released amount estimated at 42.35 % by the Weibull law fit. This feature likely occurs because the molten wax is released in cooler surrounding water that promotes its crystallization. The released and recrystallized wax can entrap still unbroken hybrid submicron capsules. Here the experiment has been performed in a cuvette without any hydrodynamic flow while in natural biological conditions (e.g. blood flow, “infinite” volume...), one can expect that this limiting effect would become limited.

### 3. Conclusion

Using a synthetic route in three steps, we produced  $\gamma\text{-Fe}_2\text{O}_3@\text{Wax}@\text{SiO}_2$  submicron capsules. The synthesis integrates the formulation of Pickering-based emulsions, inorganic chemistry to synthesize the  $\gamma\text{-Fe}_2\text{O}_3$  nanoparticles, and sol-gel chemistry to promote mineralization of the wax/water interfaces. Final hybrid object are sub-micrometer in size, with diameters around 800 nm, representing thereby the first example of submicron capsules generated by employing direct Pickering emulsions as templates. During the sol-gel process, we show that CTAB concentrations between 0.17 wt.% and 1.0 wt.% have no influence neither on the capsule size or on the silica shell thickness but strongly impact the formed silica shell density. This issue is of utmost importance as for the highest CTAB concentration (1.0 wt.%) i.e. the denser shells ( $\rho_{\text{silica}}=2.3 \text{ g}\cdot\text{cm}^{-3}$ ), whatever the heating duration and type, either magnetically-induced microscopic heat or external macroscopic source, there is no

effect on the sample morphology, which means no shell breaking. In that case, the silica shell is offering a mechanical strength high enough to sustain the wax volume expansion induced by the core melting. On the contrary, for the lower CTAB concentration (0.17 wt%), the silica shell being less dense ( $\rho_{\text{silica}}=1.3 \text{ g}\cdot\text{cm}^{-3}$ ), it cannot withstand the wax volume expansion when melting under the magnetic hyperthermia process. Thus, it is providing the expected behaviour where a magnetically-induced microscopic heat promotes the wax core melting, causing a wax volume expansion during the solid-to-liquid phase transition, and finally leading to the breaking of the surrounding silica shell. These  $\gamma\text{-Fe}_2\text{O}_3@\text{SA}@\text{Wax}@\text{SiO}_2$  capsules allow a soft wax release with time where 20 % of the wax is released after 50 minutes of hyperthermia treatment, and 40% after 2 hours. If one aims at increasing the wax release kinetics, three ways may be employed; the first one consists in increasing the iron oxide NP concentration within the wax cores, but biocompatibility issues and iron oxide over-concentration in liver would have to be considered; the second option is to design or choose nanoparticles with superior specific absorption rates, that would lead to increased heat release inside the capsules while keeping a similar overall iron oxide concentration, and the third way would be to approach more biomimetic conditions by adding a hydrodynamic flow around the capsules helping dispersing the released content. A natural outlook of this work would be to co-encapsulate hydrophobic substances of interest within the capsules, e.g. strong bioactive drugs like anti-inflammatory (Ibuprofen, Budesonide...) or anticancer drugs (Tamoxifen, Paclitaxel...). The current near-micron sizes of the capsules lay above the size of nanomedicines designed for intravenous injection. However, capsules of similar micron sizes called “microbubbles” are already used for ultrasound contrast agents or for intrapulmonary instillation.<sup>[54]</sup> Therefore hybrid  $\gamma\text{-Fe}_2\text{O}_3@\text{Wax}@\text{SiO}_2$  submicron capsules have great potential for therapeutic applications combined with bio-imaging (through the contrasting properties for magnetic resonance brought by the co-encapsulated iron oxide NPs).

## 4. Experimental Section

*Chemicals:* Diethyl ether ((C<sub>2</sub>H<sub>5</sub>)<sub>2</sub>O), hydrochloric acid 37% solution (HCl), methanol (MeOH), nitric acid 69% solution (HNO<sub>3</sub>), acetone ((CH<sub>3</sub>)<sub>2</sub>CO), ammonium hydroxide 30% solution (NH<sub>4</sub>OH), oleic acid 90% purity (C<sub>18</sub>H<sub>34</sub>O<sub>2</sub>), stearic acid 95% purity (C<sub>18</sub>H<sub>36</sub>O<sub>2</sub>), cetyltrimethylammonium bromide ((C<sub>16</sub>H<sub>33</sub>)N(CH<sub>3</sub>)<sub>3</sub>Br, CTAB), purity ≥ 98%, chloroform (CHCl<sub>3</sub>) and Sudan<sup>TM</sup> IV were purchased from Sigma-Aldrich and used as received, without further purification. Aerosil<sup>TM</sup> silica nanoparticles A380 (7 nm diameter) were provided by Evonik<sup>TM</sup>. The paraffinic wax was n-eicosane (C<sub>20</sub>H<sub>42</sub>), purity ≥ 99% ( $T_m^{\text{eicosane}}=35.9^\circ\text{C}$ , and  $\rho=0.7888\text{ g}\cdot\text{cm}^3$  in liquid state,  $\rho=0.815\text{ g}\cdot\text{cm}^3$  in solid state) from Aldrich. Tetraethoxyorthosilicate (Si(OEt)<sub>4</sub>, TEOS), purity > 99%, was the employed sol-gel alkoxide.

*Synthesis of iron oxide superparamagnetic nanoparticles:* Superparamagnetic  $\gamma\text{-Fe}_2\text{O}_3$  nanoparticles were synthesized according to Massart's procedure.<sup>[55]</sup> Magnetite Fe<sub>3</sub>O<sub>4</sub> nanocrystals (also called ferrous ferrite FeO·Fe<sub>2</sub>O<sub>3</sub>) were prepared from an aqueous alkaline coprecipitation of quasi-stoichiometric mixture of ferrous (0.9 mol) and ferric chloride (1.5 mol) salts in 100 mL of HCl solution diluted in 500 mL of water (37 wt.%). The whole solution was then further diluted with deionised water to obtain a total volume of 3 L. Under strong mechanical stirring (800 rpm), 1 L of concentrated ammonia (30 wt.%) solution was quickly added to the solution of iron ions. Coprecipitation brought up a black precipitate, characteristic of magnetite. The solution was stirred for 30 min and decanted over a magnet, until the supernatant became colorless. A strong ferrite permanent magnet (152×101×25.4 mm<sup>3</sup>, Calamit Magneti<sup>TM</sup>) was used to accelerate the particles extraction from the supernatants. After sedimentation, the flocculate was acidified with nitric acid 69% solution (360 mL) in 1.6 L of water. The obtained nanoparticles were further oxidized into maghemite using 323 g of FeNO<sub>3</sub> diluted in 800 mL of boiling water (90-100 °C) under mechanical

stirring. After this step the suspension became red, which is characteristic of maghemite  $\gamma$ - $\text{Fe}_2\text{O}_3$ . In order to remove free ions in excess, the solution was washed once with 1L of acetone and twice with 500 mL of diethyl-ether. Finally, after evaporation of residual ether by gentle heating and dispersion in water, we obtained a suspension of superparamagnetic nanoparticles stable at  $\text{pH} \approx 2$  as a true ferrofluid (i.e. remaining monophasic under the application of a magnetic field of arbitrary intensity).

*Magnetic sedimentation-based size-sorting process:* A size sorting procedure based on fractionated phase-separation was then applied on those maghemite nanoparticles in order to reduce the size-dispersity (**Figure 9**).<sup>[56]</sup> Those particles are stable in acidic water, indeed, their dipolar attractions (van der Waals and magnetic) being counterbalanced by electrostatic (double-layer) repulsion arising from the cationic charges at their surface. By addition of an excess of electrolyte, ( $\text{HNO}_3$  at  $2 \text{ mol}\cdot\text{L}^{-1}$ ), the pH decreased down to 0.8 and the ionic strength increased, thus screening electrostatic repulsions between nanoparticles. After magnetic-induced sedimentation, the two phases were macroscopically separated.

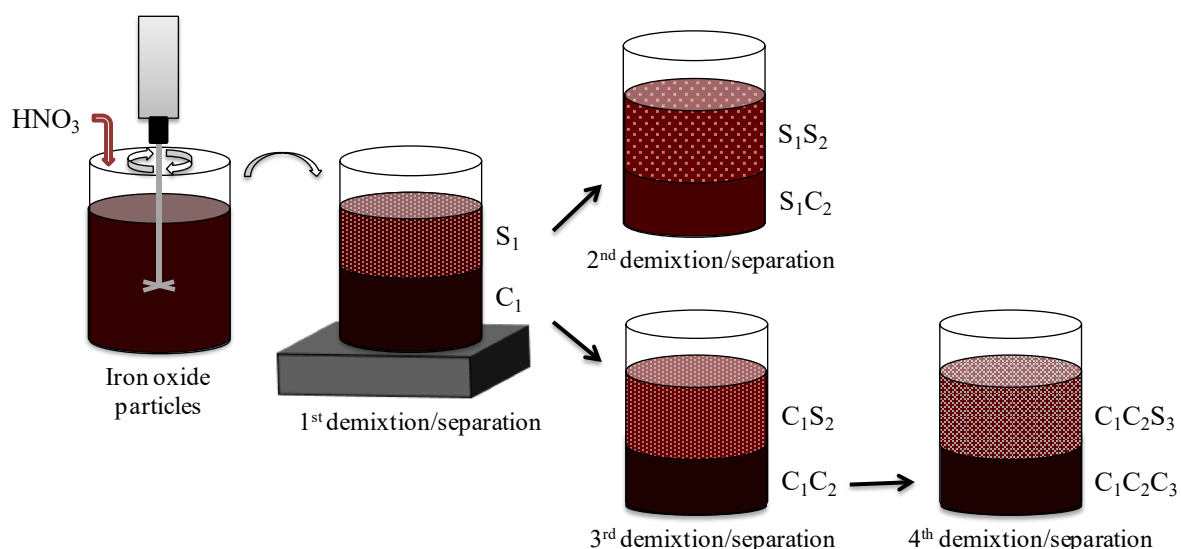


**Figure 9.** Scheme representing the steps of the size-sorting process by successive phase separation increasing the ionic strength with excess nitric acid and using a strong ferrite permanent magnet to accelerate the phase separation.

The bottom phase is named the “concentrated phase” (denoted  $C_1$ ), and is enriched in larger nanoparticles while the upper phase, named “supernatant phase” (denoted  $S_1$ ), is diluted and contains, on average, smaller nanoparticles. Then the concentrated phase was redispersed by addition of water. By repeating the size-sorting method on  $C_1$ , two new fractions were obtained at second level of refined distribution of sizes, and so on after a third level. Several fractions of refined size grades were obtained by proceeding sequential separations. Indeed, the largest batch  $C_1C_2$  was again separated in two fractions,  $C_1C_2C_3$  and  $C_1C_2S_3$ , which were washed three times by acetone and then once with diethyl ether to decrease their ionic strength and finally be redispersed in water.

*Iron content determination:* For a precise study of the magnetic heating efficiency, the value of equivalent ion concentration,  $C_{Fe}$  were obtained using total iron titration by UV-Visible spectroscopy. The iron oxide amount in nanoparticle suspension was determined from an optical absorption spectrum curve between 200 and 800 nm wavelengths, typical of the semiconductor band gap of maghemite. Quartz canisters of different light paths between 1 mm and 1 cm depending on dilution were used. This rapid and non-destructive  $C_{Fe}$  assessment can be completed by a more precise measurement involving the digestion of the nanoparticles by hydrochloric acid and their conversion into  $Fe^{3+}$  ions dissolved as a ferric complex. Each sample was incubated for 1 hour at 60 °C in HCl 5 mol·L<sup>-1</sup> in a capped vial. After an appropriate dilution to be in the linear range of the spectrometer, the iron hexachloride complex concentration,  $C_{Fe} = [FeCl_6^{3-}]$  was calculated using the Beer-Lambert’s law at the wavelength of the maximum of absorption peak of  $FeCl_6^{3-}$  (350 nm).

*Particle surface functionalization:* In order to disperse the superparamagnetic nanoparticles (NPs) into eicosane,  $C_1C_2S_3$  (fraction of interest) was coated with fatty acids of 18 carbon chain length, either oleic acid (OA) with two double bonds or stearic acid (SA), the saturated derivative, which is solid at ambient temperature. The functionalization of the iron

oxide surface occurs by chemisorption through the carboxylate surfactant end-group. For this process an equimolar mixture of fatty acid and ammonia was used, with a 5/1/1 molar ratio of iron/fatty acid/ammonia. In the case of oleic acid, the mixture was then heated at 60°C for 30 min under stirring. This black–brown mixture obtained was cooled down to room temperature ( $\approx 20^\circ\text{C}$ ) and washed three times with methanol. The end-product consisted in a dark red waxy solid, dried-out for 30 min under vacuum to remove all solvent traces. The same conditions were applied when using stearic acid, except that the temperature imposed during the process, was increased up to 70°C, i.e. just above SA melting point. Thanks to this functionalization, the iron oxide NPs became lipophilic, i.e. forming stable suspensions in molten paraffin. The coverage ratio, estimated by TGA measurements, were around 130 mg per gram of  $\gamma\text{-Fe}_2\text{O}_3$  using oleic acid coating and around 220 mg per gram of  $\gamma\text{-Fe}_2\text{O}_3$  using stearic acid for the coating. Final lipophilic iron oxide nanoparticles were labelled hereafter as  $\text{C}_1\text{C}_2\text{S}_3@\text{OA}$  and  $\text{C}_1\text{C}_2\text{S}_3@\text{SA}$  depending whether the coating is oleic acid or stearic acid. Making the maghemite surface hydrophobic is necessary to disperse the NPs into the wax core, thus enabling later on the magnetic hyperthermia heat transfer to the wax core emulsion.

*Functionalization of silica particles for stabilizing the emulsion:* In the same way, the bare silica nanoparticles used for the emulsion stabilization, are hydrophilic, therefore they do not adsorb at the eicosane-water droplets interface. For a better stabilization, we needed to confer them a stronger hydrophobic character. In this case, a very low amount of a CTAB cationic surfactant (below the CMC) was electrostatically adsorbed at the surface of Aerosil™ A380 silica NPs, which are negatively charged in water. In this case, the specific coverage area of 25 nm<sup>2</sup> per CTAB molecule at the silica surface was maintained by the CTAB/SiO<sub>2</sub> weight ratio, assuming that all the surfactant is adsorbed at the silica surface. For 7 nm-sized silica NPs, this wt. ratio has to be equal to a constant value of  $19 \times 10^{-3}$ .

*Emulsification process:* Typically, a given mass of OA- or SA-coated NPs from the  $C_1C_2S_3$  fraction was added to 18 g of eicosane to achieve a final  $12 \text{ g}\cdot\text{L}^{-1}$  concentration of iron oxide in the suspension that was heated at  $55^\circ\text{C}$  to melt the eicosane wax. Functionalized silica particles were dispersed in water at ambient temperature ( $20^\circ\text{C}$ ), and then this dispersion was also heated to  $55^\circ\text{C}$  and mixed with 18 wt.% of molten wax. Emulsification was performed using an Ultra-Turrax<sup>TM</sup> homogenizer (T25 JANKE & KUNKEL<sup>TM</sup>) equipped with an S25 N-25F rotor head at 20,000 rpm during 1 min to obtain a premix. To obtain narrower droplet size distribution, this premix was then transferred into a high-pressure homogenizer microfluidizer (MS110) from Microfluidics<sup>TM</sup> for 30 s at a given pressure of 95 MPa. During all the process, the emulsion was kept at  $55^\circ\text{C}$  to avoid wax crystallization. After stirring, the emulsion was left in an oven at  $55^\circ\text{C}$  during 10 min to let the coalescence phenomenon occur.<sup>[22]</sup> Once cooled below the wax melting temperature, a little amount (0.17 g in 5 mL of water) of CTAB-functionalized silica particles could be added to stabilize the wax dispersion for storage. Thanks to this process, 100 g of monodisperse and stable wax emulsion containing lipophilic magnetic nanoparticles were obtained.

*Pickering sub-microemulsion mineralization:* Wax dispersions were diluted from 18 to 2 wt. % by adding a CTAB solution at various concentrations (0.16, 0.5 and 1.0 wt. % CTAB with respect to the added aqueous solution). In order to catalyze the TEOS hydrolysis-condensation at the wax-water interface, while optimizing heterogeneous condensation, an HCl solution (37 vol. %) was also added to adjust the pH close to 0, below the silica isoelectric point (pH 2.1).<sup>[57]</sup> To start the mineralization, TEOS was added dropwise in different amounts (2.5, 5.0 and 7.5 mL) into 2 wt.% of wax dispersion. During all the process, the solution was placed under magnetic stirring at 450 rpm, a stirring rate unable to modify the drop size distribution. Then,  $\gamma\text{-Fe}_2\text{O}_3@\text{Wax}@\text{SiO}_2$  dispersions were placed in 50 mL test tubes under continuous stirring using a wheel rotating at 25 rpm in a thermostatically

controlled room at 20°C, and left overnight. Finally, the  $\gamma\text{-Fe}_2\text{O}_3@\text{Wax}@\text{SiO}_2$  samples were washed by cycles of centrifugation-redispersion, the successive supernatants being replaced by deionised water.

*Magnetic hyperthermia experiments:* Various concentrations (2, 4, 6 and 12 g·L<sup>-1</sup>) of iron oxide nanoparticles coated by oleic acid were incorporated into wax by dispersing the appropriate amount of “magnetic paste” in eicosane. For the stearic acid coating, only the suspension at 12 g·L<sup>-1</sup> of iron oxide nanoparticles was used. These magnetic samples either dispersed in wax bulk or in emulsified wax were exposed to a radiofrequency magnetic field created with a Seit Elettronica Junior<sup>TM</sup> induction-soldering apparatus. This MOSFET solid-state technology 3 kW generator produces a quasi-sinusoidal alternating magnetic field (AMF) at a radiofrequency  $f = 755$  kHz in the resonant circuit comprising the 4-turn induction coil (50 mm inner diameter, 32 mm height) refrigerated by an internal cold water circulation (inside the conductor wires). The AMF strength was estimated to be 10.2 kA·m<sup>-1</sup> at full power (747 V, 234 Amps) by a calibration process.<sup>[58]</sup> The macroscopic temperature was measured using a 0.42 mm diameter fiber optic sensor (OTG-M420, Opsens<sup>TM</sup>) passed through a hole in the cap of the quartz canister (Hellma<sup>TM</sup> 105 QS) filled with 400  $\mu\text{L}$  of sample. The standard process is such that the sample temperature is first adjusted at an initial value above room temperature but below the melting temperature of eicosane, using an external water circulation with a thermostatic bath (Huber Polystat<sup>TM</sup> CC) through a double-wall glass jacket located inside the coil, until a plateau is reached. Then the magnetic field is applied until another plateau is reached, corresponding to a perfect compensation of the heat powers respectively generated by the sample and dissipated into the surrounding medium, or the latent heat that the wax absorbs to undergo solid to liquid phase transition.

*Characterization techniques:* In order to determine the concentration of iron oxide, a thermogravimetric analysis (TGA) was used to know the inorganic vs. organic contents in the

total solid matter, and thus, the weight fraction of iron oxide when incorporating a given weight of fatty acid-coated waxy powder in eicosane. The TGA was performed with a Setaram Instrumentation™ thermal balance, using airflow and a temperature ramp of 10 °C/min from 20 to 800°C. Aggregation state of the dispersions was characterized by optical microscopy using an inverted optical microscope Zeiss™ Axiovert™ X100. Images were recorded using a Hitachi video camera and a Scion frame-grabber using ImageJ program. Scanning electron microscopy (SEM) pictures were captured with a Hitachi TM-1000 apparatus and with a Hitachi S2500 to allow a resolution, up to the nanometer scale. Transmission electron microscopy (TEM) was also performed, with a Hitachi H600 TEM operated at 100 kV, to estimate the shell thickness of the obtained capsules. Suspensions were previously dried at ambient temperature or were lyophilized using an Alpha 2-4 LD Plus freeze-dryer after freezing for one night at -80 °C. For SEM observations, all samples were sputtered with gold before observation.

Two kinds of instruments were employed for the assessment of the hydrodynamic diameters by dynamic light scattering (DLS). In order to determine the size of the fatty acid-coated iron oxide NPs, the different suspensions of iron oxide at  $\approx 0.1 \text{ g}\cdot\text{L}^{-1}$  in eicosane were analyzed with a photon correlation system (CGS-5000 from ALV GmbH) at a scattering angle of 90°. For iron oxide NPs suspensions, the temperature was set at 20°C in a mix water/HNO<sub>3</sub> (pH  $\approx$  2). Analysis of the data during the AMF experiments was performed using the refraction index of eicosane (1.4355) at the liquid state. Therefore, viscosity  $\eta$  (mPa·s<sup>-1</sup>) is following the experimental scaling law with temperature  $T$  (in °C):  $\eta = 47.70 \times T^{-0.5533}$  (**Supporting Information, Figure S7**). This technique was also used for the emulsion droplet sizing, using the viscosity and index of refraction of water as suspending medium. The size distribution is obtained after three measurements just after emulsification at 60°C. During the alternating magnetic field (AMF) application, *in situ* measurements were acquired

simultaneously using the VASCO Flex™ remote-head DLS instrument developed by Cordouan Technologies, working at a scattering angle of 165° i.e. in backscattering with fiber optics and an avalanche diode as photodetector. After choosing the minimum decay time (typically 8–20  $\mu$ s) and number of channels of the correlator (450– 900), the acquisition was launched for an unlimited time with independent sub-runs of 30 s. For each of the sub-runs all along the experiment, the associated correlogram was analyzed by both the 2<sup>nd</sup> order cumulant and the Padé-Laplace fitting methods. The macroscopic temperature was also simultaneously recorded by the Opsens conditioner (through a RS-232 cable) and by the Cordouan NanoQ™ 2.5 software, through an analog output that was protected from the electromagnetic perturbations, when the AMF was on, with a shielded cable. The operator him/herself was also protected from the AMF and the high voltage by placing all the experiment in a metallic box acting as a Faraday cage.

Thermal analyses were conducted, through Differential Scanning Calorimetry (DSC), using a TA-Q2000 DSC apparatus. TA Instrument™ Explorer software was used to record the measurements and TA Universal Analysis™ software to analyze all the results. The melting temperature ( $T_m$ ) of the samples was determined following two protocols based on temperature cycles of +20°C to +60°C according to variable speeds. As usual when working with alkane chain transitions, we launched a first program, called throughout our study "quick method", which measures the heat flow  $Q$  at a speed of  $\pm 2^\circ$  C/min. To assess the influence of heat on the crystallization, we also conducted a second program called "slow method" where the speed was reduced to  $\pm 0.2^\circ$  C/min. We decided to take, as a melting temperature, the onset which is the temperature value corresponding to the intersection of the tangent between the inflection point of the curve and the baseline, indicating the transition temperature much more accurately than from the peak.

Wide angle X-ray scattering (WAXS) data were collected on a Rigaku Nanoviewer™ (XRF

microsource generator, MicroMax<sup>™</sup> 007HF), with a 1200-W rotating anode coupled to a confocal Max-Flux<sup>®</sup> Osmic<sup>™</sup> mirror (Applied Rigaku Technologies) and a MAR345 image plate detector (MARResearch). Samples were put in Lindemann glass capillaries, which were exposed to the X-Ray beam. The detector was placed at a distance of 309 mm from the sample providing access to  $2\theta$  angles in the  $0.5 - 29^\circ$  range. The capillary was held in an oven enabling to reach high temperature regulated by a proportional–integral–derivative (PID) controller. Helium pycnometry was used to determine the volumetric mass density of silica shells by measuring the pressure change in a calibrated gas volume. The results were recorded with an Accupyc<sup>™</sup> 1330 pycnometer from Micromeritics, which operates by following Mariotte’s gas law:  $P_1V_1 = P_2V_2$  where  $P_1$  is the pressure in the cell,  $V_1$  the cell volume,  $P_2$  the pressure in the expansion circuit and  $V_2$  the expansion volume.

Small angle neutron scattering (SANS) measurements were performed on the PACE spectrometer of the Laboratoire Léon Brillouin (CEA-Saclay, France). MNP dispersions in either acidic water ( $\text{HNO}_3$  pH~2) or eicosane were prepared at  $12 \text{ mg}\cdot\text{mL}^{-1}$  of  $\gamma\text{-Fe}_2\text{O}_3$  and at a temperature of  $60^\circ\text{C}$  to be in the melted state of the wax. Three beamline configurations were used to cover overlapping scattering vector ( $q$ ) ranges of  $3.2\times 10^{-3} - 3.4\times 10^{-2}$ ,  $1.1\times 10^{-2} - 0.12$ , and  $3.6\times 10^{-2} - 0.37 \text{ \AA}^{-1}$ , with the following values of sample-to-detector distance  $D$  and neutron wavelength  $\lambda$ :  $D=4.57 \text{ m}$  and  $\lambda=13 \text{ \AA}$ ,  $D=2.85 \text{ m}$  and  $\lambda=6 \text{ \AA}$ ,  $D=0.87 \text{ m}$  and  $\lambda=6 \text{ \AA}$ . Analysis of the scattering intensity curves aims at obtaining the characteristic sizes, shape and inter-NP interactions, represented respectively by the form factor  $P(q)$  and the structure factor  $S(q)$ . These functions were simulated by analytical models using SasView 3.1.2 software (<http://sasview.org>): The  $P(q)$  of polydisperse spheres was used to fit the curve of C1C2S3 NPs in water, while a core-shell  $P(q)$  model was used for the coated C1C2S3@SA NPs in eicosane. For both of them, a “stick hard sphere” model was used for  $S(q)$  in order to simulate short-range attractive interactions between the NPs.<sup>[59,60]</sup> Other details of the SANS analysis

are given in the legend of **Figure S8 in Supporting Information**.

### **Acknowledgements**

All the co-authors contributed equally to this work. Co-authors thank Ahmed Bentaleb for technical assistance with the AMF generator electronics and for X-ray measurement of eicosane study, Eric Laurichesse for rheological measurement of eicosane versus temperature and Louis Beaute for the synthesis of the iron oxide nanoparticles.

### **References**

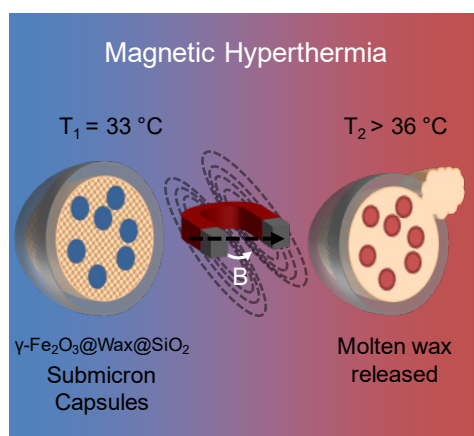
- [1] D. Schmaljohann, *Adv. Drug Deliv. Rev.* **2006**, *58*, 1655.
- [2] S. Ganta, H. Devalapally, A. Shahiwala, M. Amiji, *J. Control. Release* **2008**, *126*, 187.
- [3] L. Kromidas, E. Perrier, J. Flanagan, R. Rivero, I. Bonnet, *Int. J. Cosmet. Sci.* **2006**, *28*, 103.
- [4] T. Lotan, S. Eckhouse, *Methods Compositions and Devices Utilizing Stinging Cells/capsules for Delivering a Therapeutic or a Cosmetic Agent into a Tissue*, **2013**.
- [5] S. P. Friedman, Y. Mualem, *Fertil. Res.* **1994**, *39*, 19.
- [6] Y. Wada, K. Isono, Y. Otsu, S. Sone, K. Hanaki, T. Abe, *Capsule Preparations for Plant Treatment*, **1999**.
- [7] M. Nollet, M. Mercé, E. Laurichesse, A. Pezon, O. Soubabère, S. Besse, V. Schmitt, *Soft Matter* **2016**, *12*, 3412.
- [8] A. P. Esser-Kahn, S. A. Odom, N. R. Sottos, S. R. White, J. S. Moore, *Macromolecules* **2011**, *44*, 5539.
- [9] A. Angelova, B. Angelov, S. Lesieur, R. Mutafchieva, M. Ollivon, C. Bourgaux, R. Willumeit, P. Couvreur, *J. Drug Deliv. Sci. Technol.* **2008**, *18*, 41.
- [10] S. Daoud-Mahammed, C. Ringard-Lefebvre, N. Razzouq, V. Rosilio, B. Gillet, P. Couvreur, C. Amiel, R. Gref, *J. Colloid Interface Sci.* **2007**, *307*, 83.
- [11] W.-H. Chen, S. L. Regen, *J. Am. Chem. Soc.* **2005**, *127*, 6538.
- [12] A. D. Dinsmore, M. F. Hsu, M. G. Nikolaides, M. Marquez, A. R. Bausch, D. A. Weitz, *Science (80-. )*. **2002**, *298*, 1006.
- [13] O. D. Velev, K. Furusawa, K. Nagayama, *Langmuir* **1996**, *12*, 2374.
- [14] M. Baillot, A. Bentaleb, E. Laurichesse, V. Schmitt, R. Backov, *Langmuir* **2016**, *32*, 3880.
- [15] M. O'Sullivan, Z. Zhang, B. Vincent, *Langmuir* **2009**, *25*, 7962.
- [16] G. Fornasieri, S. Badaire, R. Backov, O. Mondain-Monval, C. Zakri, P. Paulin, *Adv. Mater.* **2004**, *16*, 1094.

- [17] H. Gao, W. Yang, K. Min, L. Zha, C. Wang, S. Fu, *Polymer (Guildf)*. **2005**, *46*, 1087.
- [18] K. Kawaguchi, in *Microspheres, Microcapsules and Liposomes* (Ed.: R. Arshady), Citus Books, Londres, **1999**, pp. 125–163.
- [19] S. Q. Liu, Y. Y. Yang, X. M. Liu, Y. W. Tong, *Biomacromolecules* **2003**, *4*, 1784.
- [20] S. Jämsä, R. Mahlberg, U. Holopainen, J. Ropponen, A. Savolainen, A. C. Ritschkoff, *Prog. Org. Coatings* **2013**, *76*, 269.
- [21] M. Volz, P. Walther, U. Ziener, K. Landfester, *Macromol. Mater. Eng.* **2007**, *292*, 1237.
- [22] M. Destribats, V. Schmitt, R. Backov, *Langmuir* **2009**, *26*, 1734.
- [23] S. U. Pickering, *J. Chem. Soc. Trans.* **1907**, *91*, 2001.
- [24] B. P. Binks, *Curr. Opin. Colloid Interface Sci.* **2002**, *7*, 21.
- [25] R. Backov, *Soft Matter* **2006**, *2*, 452.
- [26] M. Nollet, M. Depardieu, M. Destribats, R. Backov, V. Schmitt, *Part. Part. Syst. Charact.* **2013**, *30*, 62.
- [27] M. Depardieu, M. Nollet, M. Destribats, V. Schmitt, R. Backov, *Part. Part. Syst. Charact.* **2013**, *30*, 185.
- [28] S. Mornet, S. Vasseur, F. Grasset, E. Duguet, *J. Mater. Chem.* **2004**, *14*, 2161.
- [29] E. A. Périgo, G. Hemery, O. Sandre, D. Ortega, E. Garaio, F. Plazaola, F. J. Teran, *Appl. Phys. Rev.* **2015**, *2*, DOI 10.1063/1.4935688.
- [30] M. Bonini, D. Berti, P. Baglioni, *Curr. Opin. Colloid Interface Sci.* **2013**, *18*, 459.
- [31] C. S. Brazel, *Pharm. Res.* **2009**, *26*, 644.
- [32] E. Guisasaola, A. Baeza, M. Talelli, D. Arcos, M. Vallet-Regí, *RSC Adv.* **2016**, *6*, 42510.
- [33] E. Loiseau, A. Q. de Boiry, F. Niedermair, G. Albrecht, P. A. Rühls, A. R. Studart, *Adv. Funct. Mater.* **2016**, *26*, 4007.
- [34] T. Fontecave, M. Bourbousson, C. Chaneac, C. Wilhelm, A. Espinosa, M. A. Fortin, C. Sanchez, C. Boissiere, *New J. Chem.* **2016**, *40*, 4436.
- [35] R. M. Wiley, *J. Colloid Sci.* **1954**, *9*, 427.
- [36] S. Arditty, C. P. Whitby, B. P. Binks, V. Schmitt, F. Leal-Calderon, *Eur. Phys. J. E* **2003**, *11*, 273.
- [37] M. Destribats, B. Faure, M. Birot, O. Babot, V. Schmitt, R. Backov, *Adv. Funct. Mater.* **2012**, *22*, 2642.
- [38] J. Giermanska-Kahn, V. Laine, S. Arditty, V. Schmitt, F. Leal-Calderon, *Langmuir* **2005**, *21*, 4316.

- [39] V. SCHMITT, J. Kahn, S. RECLUSUSA, S. Ravaine, C. F. Leal, S. Arditty, **2005**.
- [40] V. Schmitt, J. Kahn, S. Reculusa, S. Ravaine, F. Leal-Calderon, S. Arditty, *Crystallisable Oil Compositions Stabilised by Solid Colloidal Particles*, **2005**, WO2005082507 A1.
- [41] F. Thivilliers, N. Drelon, V. Schmitt, F. Leal-Calderon, *Europhys. Lett.* **2006**, *76*, 332.
- [42] K. Boode, P. Walstra, *Colloids Surfaces A Physicochem. Eng. Asp.* **1993**, *81*, 121.
- [43] M. A. J. S. van Boekel, P. Walstra, *Colloids and Surfaces* **1981**, *3*, 109.
- [44] N. Denkov, S. Tcholakova, I. Lesov, D. Cholakova, S. K. Smoukov, *Nature* **2015**, *528*, 392.
- [45] C. Y. Chen, S. Q. Xiao, M. E. Davis, *Microporous Mater.* **1995**, *4*, 1.
- [46] S. Andersson, L. Dzhavadov, *J. Phys. Condens. Matter* **1992**, *4*, 6209.
- [47] J. C. Van Miltenburg, H. A. J. Oonk, V. Metivaud, *J. Chem. Eng. Data* **1999**, *44*, 715.
- [48] W. Wang, C. Wang, W. Li, X. Fan, Z. Wu, J. Zheng, X. Li, *Phys. Chem. Chem. Phys.* **2013**, *15*, 14390.
- [49] E. F. Westrum Jr., F. Grønvold, *J. Chem. Thermodyn.* **1969**, *1*, 543.
- [50] M. Mercé, H. Saadaoui, F. Dole, L. Buisson, A. Bentaleb, D. Ruggi, V. Schmitt, R. Backov, *J. Mater. Sci.* **2015**, *50*, 6586.
- [51] C. Di Giambattista, R. Sanctuary, E. Perigo, J. Baller, *J. Chem. Phys.* **2015**, *143*, DOI 10.1063/1.4928059.
- [52] M. S. Lobo, P. Costa, **2001**, *13*, 123.
- [53] K. Kosmidis, P. Argyrakis, **2003**, *20*, 988.
- [54] E. Pisani, N. Tsapis, B. Galaz, M. Santin, R. Berti, N. Taulier, E. Kurtisovski, O. Lucidarme, M. Ourevitch, B. T. Doan, J. C. Beloeil, B. Gillet, W. Urbach, S. L. Bridal, E. Fattal, *Adv. Funct. Mater.* **2008**, *18*, 2963.
- [55] R. Massart, *Magn. IEEE Trans.* **1981**, *17*, 1247.
- [56] R. Massart, E. Dubois, V. Cabuil, E. Hasmonay, *J. Magn. Magn. Mater.* **1995**, *149*, 1.
- [57] C. J. Brinker, G. W. Scherer, *Sol-Gel Science: The Physics and Chemistry of Sol-Gel Processing*, **1990**.
- [58] G. Hemery, E. Garanger, S. Lecommandoux, A. D. Wong, E. R. Gillies, B. Pedrono, T. Bayle, D. Jacob, O. Sandre, *J. Phys. D. Appl. Phys.* **2015**, *48*, DOI 10.1088/0022-3727/48/49/494001.
- [59] R.J. J. Baxter, *Chem. Phys.* **1968**, *49*, 2770.
- [60] S. V. G. Menon, C. Manohar, K. S. Rao, *J. Chem. Phys.* **1991**, *95*, 9186.

## The table of contents entry

**Thermo-magnetically responsive  $\gamma\text{-Fe}_2\text{O}_3\text{@Wax@SiO}_2$  submicron capsules are designed** through the *integrative chemistry*-based coupling of Pickering emulsions and sol-gel chemistry. Here, the magnetically-induced heating provided by the  $\gamma\text{-Fe}_2\text{O}_3$  internal magnetic moments is sufficient to melt the wax core, expanding its volume, inducing thereby the surrounding silica shell rupture, where 20wt% of the wax is being released after 50 minutes of alternating magnetic field (AMF) treatment.



## Supporting Information

### Thermo-Magnetically Responsive $\gamma$ -Fe<sub>2</sub>O<sub>3</sub>@Wax@SiO<sub>2</sub> Submicron Capsules

*M. Baillot,<sup>[1]</sup> G. Hemery,<sup>[2]</sup> O. Sandre,<sup>[2]</sup> V. Schmitt<sup>[1,\*]</sup> and R. Backov<sup>[1,\*]</sup>*

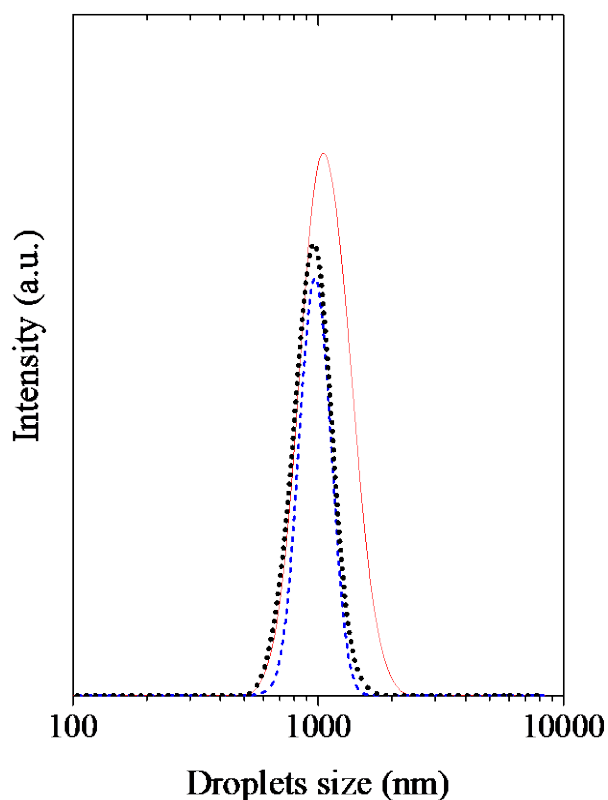


**Figure S1.** DLS spectra of eicosane emulsion on 1<sup>st</sup>, 3<sup>rd</sup> and 7<sup>th</sup> days. The red line corresponds to the spectra at 1 day, the blue dashed line corresponds to the spectra on the 3<sup>rd</sup> and the dark dotted line corresponds to the spectra on the 7<sup>th</sup> day.

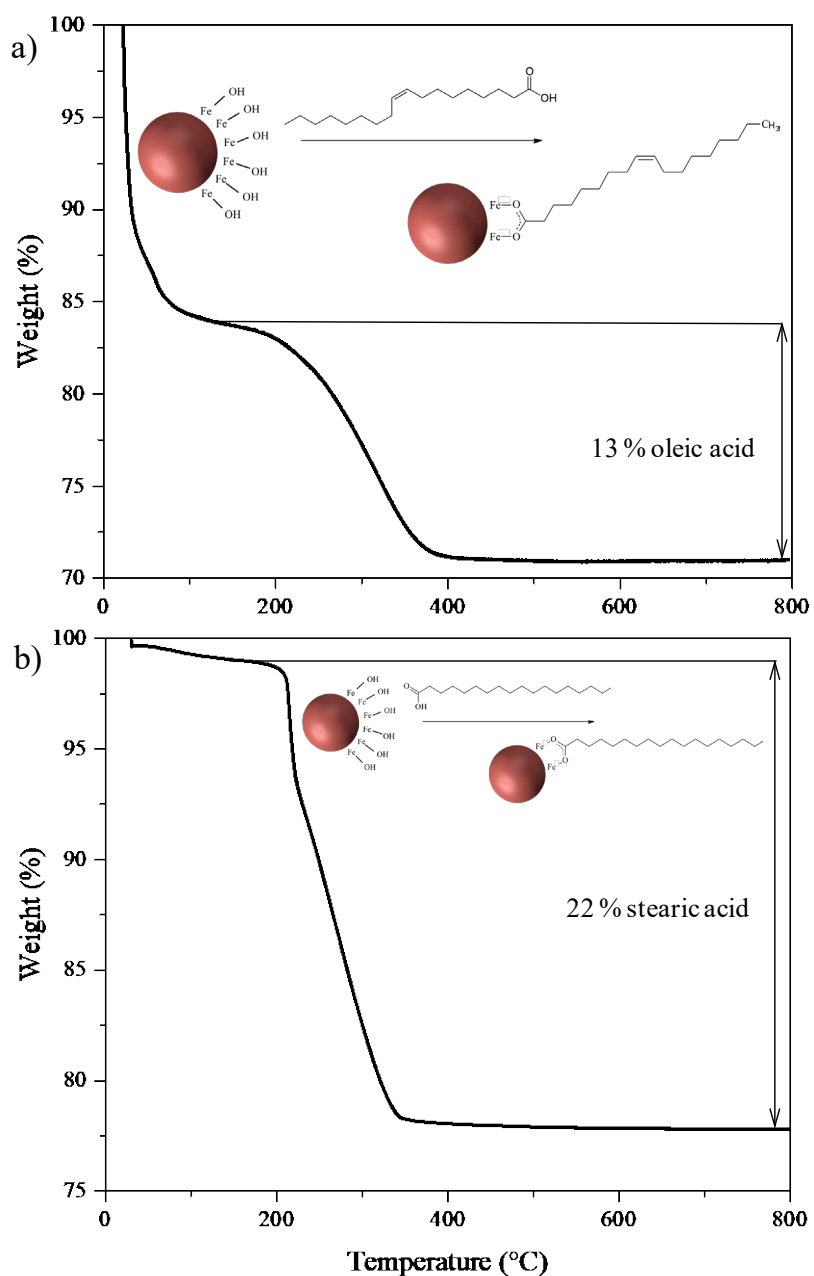


**Figure S2.** TGA thermograms between 20 and 800°C in air for a)  $C_1C_2S_3@OA$  and b)  $C_1C_2S_3@SA$  NPs to determine the organic content in the magnetic paste samples. Mass losses below 120°C correspond to remaining hydration water, while the gaps between 180°C and 800°C can be ascribed to the degradation of organic matter. Schemes of the coating process of an iron oxide particle by oleic acid and stearic acid are also represented.

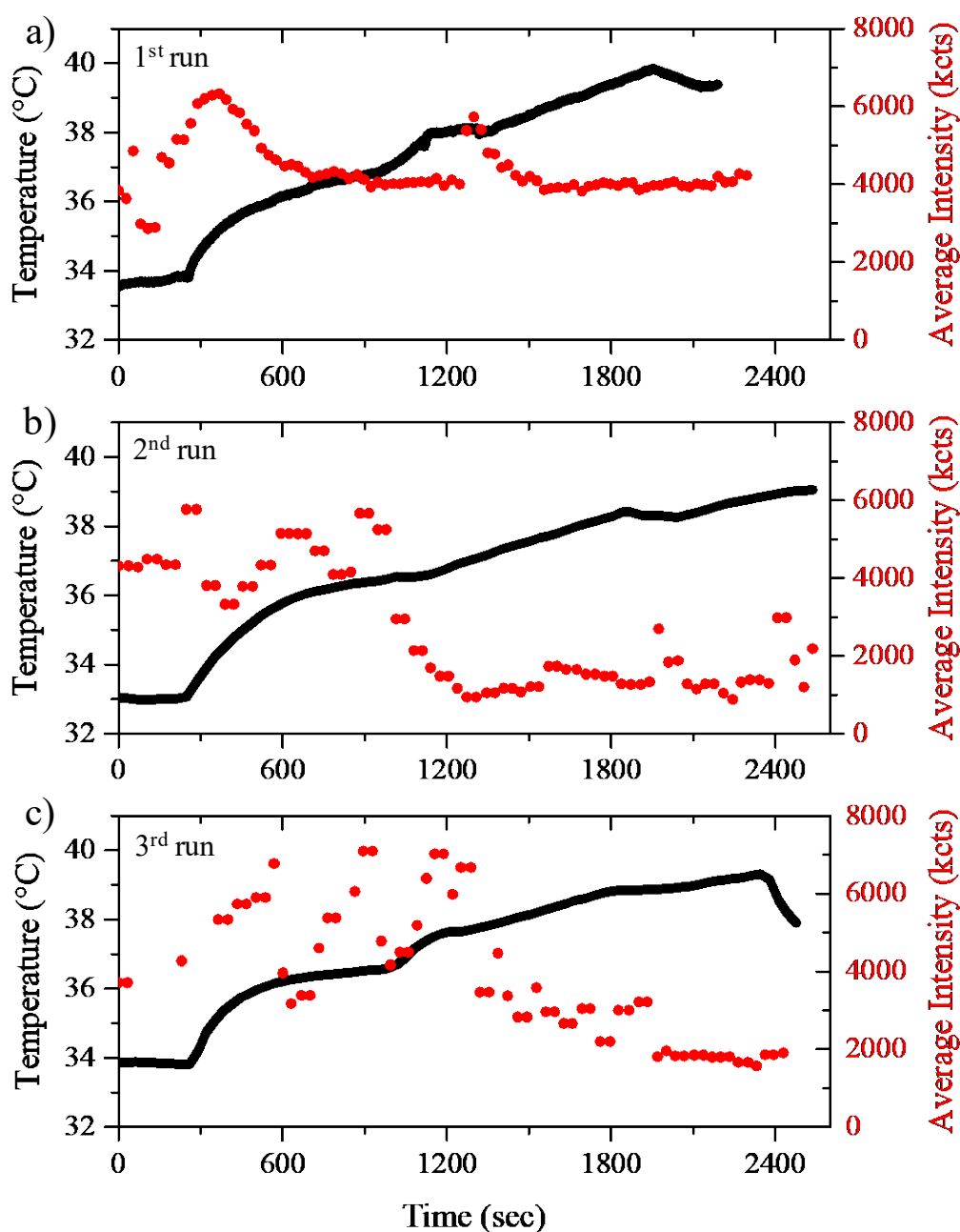


**Figure S3.** Three runs of AMF application (magnetic field  $10.2 \text{ kA}\cdot\text{m}^{-1}$  at  $755 \text{ kHz}$ ) on bulk eicosane samples ( $300 \mu\text{L}$ ) containing grafted iron oxide nanoparticles at  $12 \text{ g}\cdot\text{L}^{-1}$ . Temperature was initially stabilized at  $\approx 33.5^\circ\text{C}$  using a glass double-wall water jacket thermalized by circulating water at  $37^\circ\text{C}$ . a) first run, b) second run and c) third run. Black lines correspond to the temperature measured by an optical fiber thermometer placed in the sample. Red dots correspond to the average backscattered light intensity of the laser beam of the DLS remote head giving additional information on the phase changes of the wax.

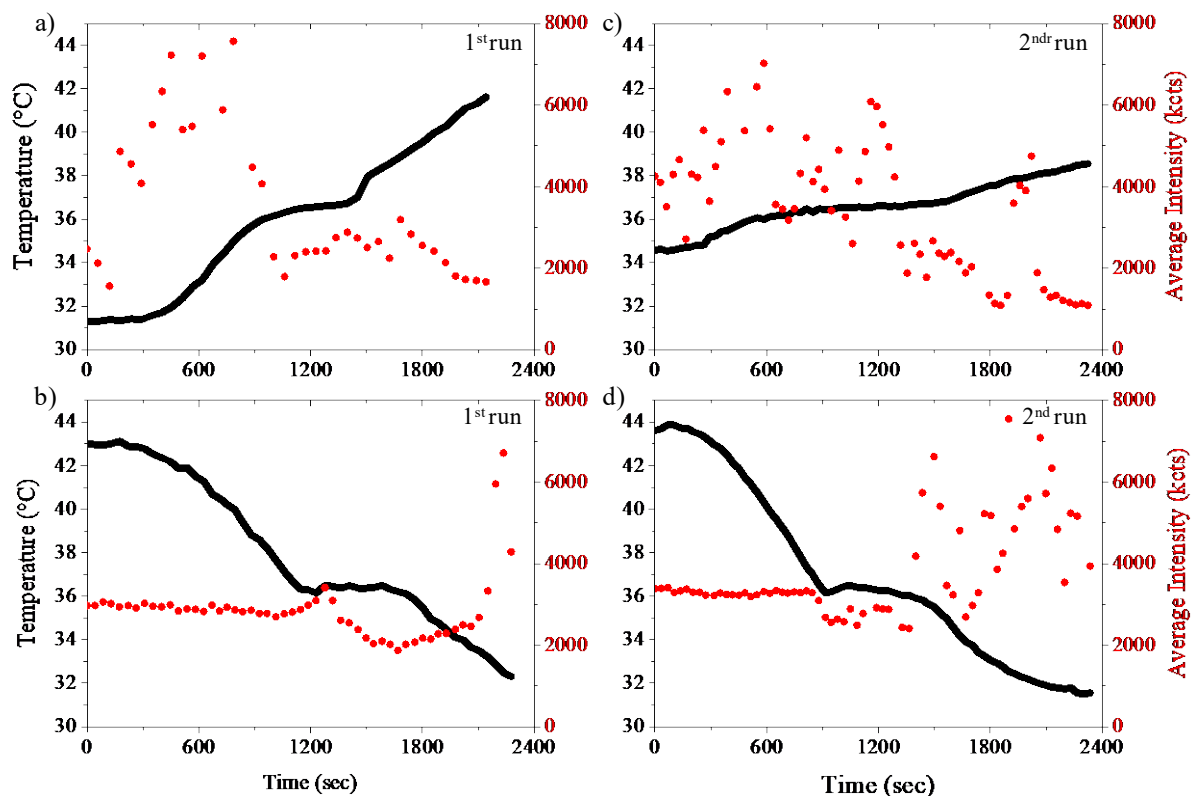


**Figure S4.** Two runs of direct (non-magnetic) heating (a and b, heating rate of 2.9°C per minute) and cooling (c and d) of bulk eicosane containing SA-grafted iron oxide NPs at 12 g·L<sup>-1</sup>, after stabilization of the sample temperature using a glass double-wall water-jacket. Black lines correspond to the temperature of the sample. Red dots correspond to the average backscattered light intensity of the laser beam of the DLS remoted head giving additional information on the phase changes of the wax.

In order to determine directly the influence of the iron oxide nanoparticles on eicosane structure, power X-ray diffractograms of eicosane were obtained every degree of temperature between 32 and 40°C (**Figure S5**).

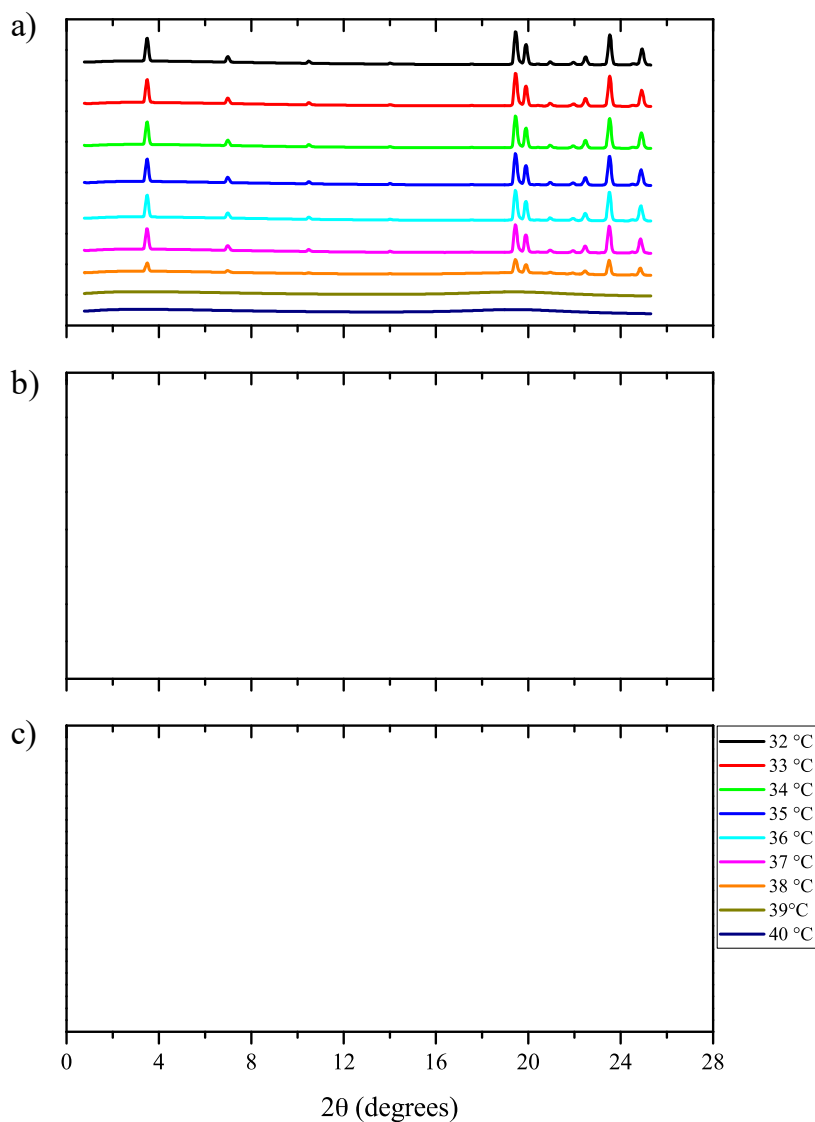


**Figure S5.** X-Ray diffractograms of eicosane every degree of temperature between 32 and 40 °C obtained after three runs of heating with an oven placed on WAXS assembly corresponding to a) first run, b) second run and c) third run. The heating rate was set to 0.2°C per minute.

X-ray scattering peaks regularly spaced at small angles indicate that the wax presents a lamellar structure  $L_1$ , with a  $d_{002}$  spacing of 50.5 Å. It is perfectly identical for each run carried out between 32 and 38°C (**Figure S5.a-c**). This structure disappears in favour of a totally amorphous one at 39°C. It means that the wax melts between 38 and 39°C. Thus, there

is a gap about the melting temperature of eicosane detected by WAXS and by DSC experiments, explained by a loss of heat between the sample and the oven temperature. We may also argue that the exact melting temperature could differ from different heating rates applied during the DSC and the WAXS experiments, but in the present case the heating rate was the same and set to 0.2°C/min. We reproduced this experience twice (**Figure S5.b-c**) on the same sample after cooling. For the second run (**Figure S5.b**), at  $T < 34^\circ\text{C}$ , a second structure appeared, being also lamellar it is denoted "L<sub>2</sub>", with a higher  $d_{002}$  spacing of 53.5 Å. At  $T > 34^\circ\text{C}$ , the wax biphasic nature disappears leading to the same one obtained during the first run, while the transition toward an amorphous phase is occurring again above 38°C. However, during the third run, the initial monophasic L<sub>1</sub> structure was detected for each temperature between 32 and 39°C, meaning that the L<sub>2</sub> phase is a presumably a metastable phase, i.e. kinetically but not thermodynamically favourable. Indeed, when  $T > 39^\circ\text{C}$  we observed the transition toward the amorphous phase with only a bump corresponding to the average distance between molecules in the liquid phase. Despite the fact that we observed the same initial L<sub>1</sub> lamellar structure than the first run, the eicosane melting temperature evolved from 38 to 39°C after three runs. It has been demonstrated that eicosane evolves through metastable rotator phases when reaching the melting temperature, and this phenomenon of "pre-transition" increases the apparent heat capacities due to a latent heat effect.<sup>1</sup> The space group of the rotator phases, located between 18-25° and corresponding to the crystallographic directions (111) and (020), is face-centred orthorhombic, but with temperature, the structure showed an hexagonal distortion parameter D (depending on the lattice parameters a, b, and c).

Diffraction patterns of eicosane, containing iron particles (12 g·L<sup>-1</sup>) grafted with oleic acid, were obtained at each degree of temperature between 32 and 40°C (**Figure S6**). It appears that the presence of iron particles into the eicosane did not alter its structure. Indeed, the X-

---

<sup>1</sup> Di Giambattista, C.; Sanctuary, R.; Périgo, E.; Baller, J., *J. Chem. Phys.* **2015**, *5*, 143.

Ray diffractograms are identical to the ones obtained without iron particles (**Figure S6.a-c**). In particular, the Bragg peaks of the iron oxide maghemite phase cannot be seen since they are located at  $2\theta$  values above  $30^\circ$ .<sup>2</sup>

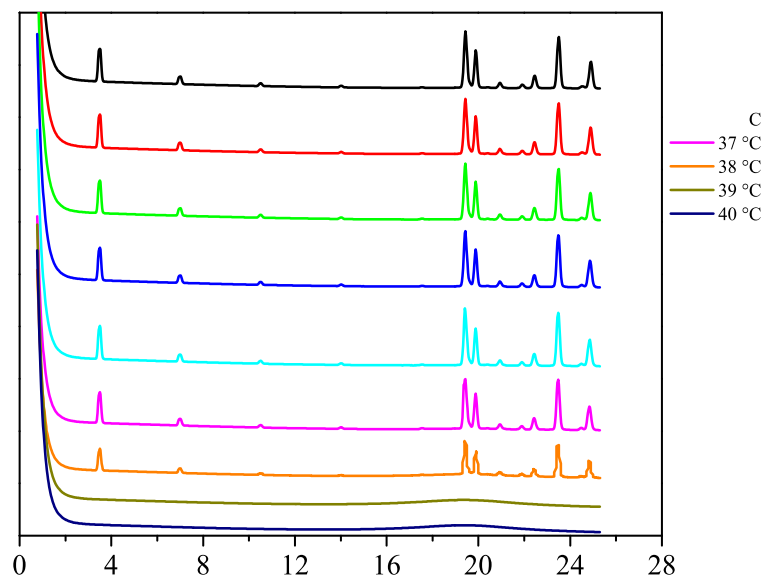


**Figure S6.** X-ray diffractograms of eicosane containing iron particles ( $12 \text{ g}\cdot\text{L}^{-1}$ ), for each degree of temperature between 32 and  $40^\circ\text{C}$ , heating it in an oven at a heating rate of  $0.2^\circ\text{C}\cdot\text{min}^{-1}$ .

<sup>2</sup> R. Cornell, U. Schwertmann, *The Iron Oxides: Structure, Properties, Reactions, Occurrences and Uses*, Wiley-VCH Verlag GmbH & Co. KGaA, **1996**.

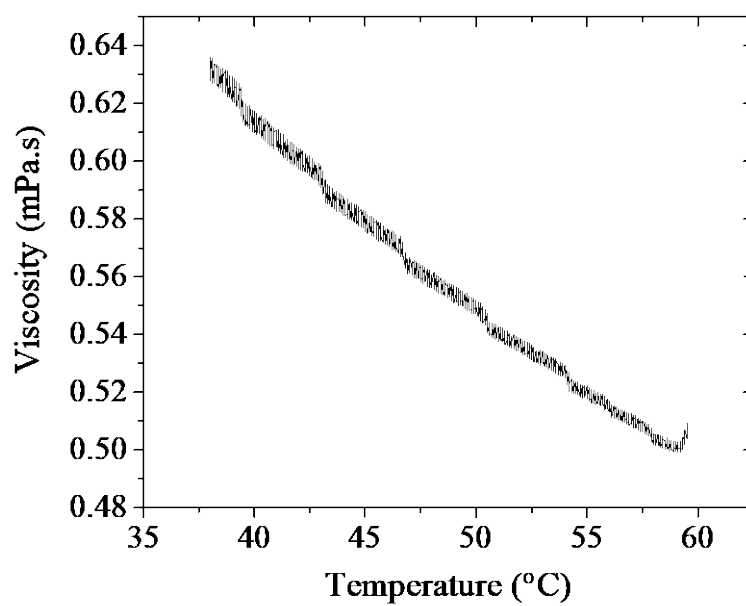


**Figure S7.** Eicosane viscosity as a function of temperature in the liquid phase from 38 to 60°C. The experiment has been carried out using an AR200 Instruments and applying a 1°C·min<sup>-1</sup> temperature ramp.

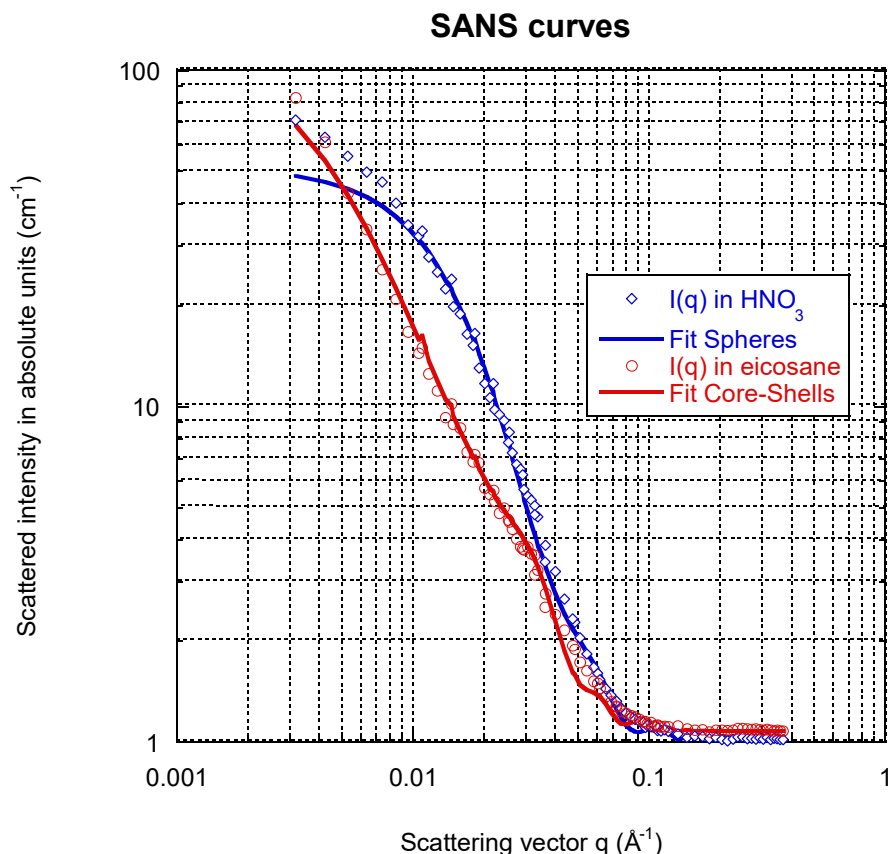


**Figure S8.** Small angle neutron scattering (SANS) curves of the bare C1C2S3  $\gamma$ -Fe<sub>2</sub>O<sub>3</sub> NPs MNPs dispersed in weakly acidic aqueous medium (pH~2) and of the grafted C1C2S3@SA NPs dispersed in eicosane. Both experiments were performed at 12 g·L<sup>-1</sup>  $\gamma$ -Fe<sub>2</sub>O<sub>3</sub> and 60°C. The solid lines represent simulated using SasView 3.1.2 software (<http://sasview.org>) with respectively the polydisperse sphere and the core-shell form factors both multiplied by a “sticky hard sphere” structure factor to take into account attractive interactions between NPs. More precisely, the calculated neutron scattering length densities of the different components were:  $SLD(\gamma\text{-Fe}_2\text{O}_3)=6.98\times 10^{-6}$  Å<sup>-2</sup>,  $SLD(\text{H}_2\text{O})=-5.6\times 10^{-7}$  Å<sup>-2</sup>,  $SLD(\text{C}_{20}\text{H}_{42})=-4.99\times 10^{-7}$  Å<sup>-2</sup>, and  $SLD(\text{SA})=-6.71\times 10^{-8}$  Å<sup>-2</sup>. Volume fractions were  $\phi=0.0024$  for the acidic water suspension and  $\phi=0.0031$  for C1C2S3@SA in eicosane. They were calculated from the 12 g·L<sup>-1</sup> weight concentration and the respective volumetric mass densities: 5 g·cm<sup>-3</sup> for  $\gamma$ -Fe<sub>2</sub>O<sub>3</sub> and 0.775 g·cm<sup>-3</sup> for liquid eicosane. One constraint of the fitting procedure was to maintain an identical log-normal distribution law for the  $\gamma$ -Fe<sub>2</sub>O<sub>3</sub> core radii. Although polydisperse, the best fitting value was  $R=25.1\pm 17.8$  Å ( $\sigma=0.56$ ). For the coated NPs, the thickness of SA layer was also varied to optimize the fit, yielding  $H=15.4\pm 5$  Å ( $\sigma=0.20$ ), a plausible value for a fatty acid monolayer. Other fitting parameters of the sticky hard sphere structure factor were the “stickiness”  $\tau=0.078\pm 0.00063$  (respectively  $\tau=-0.011\pm 0.0089$ ) and the “perturbation distance”  $\varepsilon=0.543\pm 0.0019$  (respectively  $\varepsilon=1.397\pm 0.040$ ) for the uncoated (respectively coated) C1C2S3 NPs. These non-dimensioned parameters represent the attraction potential ( $\tau$ ) and capture distance ( $\varepsilon$ ) between the NPs. The deviation between the fitted curve and the experimental data points at low  $q$  vectors for the uncoated  $\gamma$ -Fe<sub>2</sub>O<sub>3</sub> NPs is likely ascribed to a small degree of aggregation. Despite the relative large size-dispersity parameter ( $\sigma=0.56$ ) for the C1C2S3 NPs, an average radius  $R_{\text{SANS}}=5.5$  nm (diameter of 11 nm) could be calculated using the Porod regime of the curves. The intensity in the high  $q$  region can indeed be

approximated by the Porod law:  $[I(q) - I_{\text{background}}] \cdot q^4 = 2\pi\phi(1 - \phi)(\Delta SLD)^2 \cdot 3/R_{\text{SANS}}$  where  $\Delta SLD$  stands for the neutron scattering contrast, *i.e.* the difference of  $SLD$  value between the  $\gamma\text{-Fe}_2\text{O}_3$  cores and the medium (here liquid eicosane  $\text{C}_{20}\text{H}_{42}$ ). The specific area is given by  $S_{\text{spe}} = 3/R_{\text{SANS}}/\rho$ , where  $\rho$  is the volumetric mass density of  $\gamma\text{-Fe}_2\text{O}_3$  ( $5 \text{ g}\cdot\text{cm}^{-3}$ ). Experimentally,  $S_{\text{spe}} \sim 110 \text{ m}^2\cdot\text{g}^{-1}$  was obtained from the high  $q$  regime of the intensity curve of C1C2S3@SA NPs in eicosane.